# Nanoimprint Lithography and its Applications in Photonics, Biotechnology and Energy Conversion Devices

**by**

**Brandon D. Lucas**

**A dissertation submitted in partial fulfillment**
**of the requirements for the degree of**
**Doctor of Philosophy**
**(Applied Physics)**
**in the University of Michigan**
**2017**

**Doctoral Committee:**

Professor L. Jay Guo, Chair
Professor Cagliyan Kurdak
Assistant Professor Xiaogan Liang
Associate Research Scientist Moussa N'Gom

## DEDICATION

This is dedicated to everyone that has supported me along this journey. I thank God for your presence and support in my life!

## ACKNOWLEDGMENTS

I would like to thank my committee for their support throughout this process. A special expression of gratitude to my advisor Professor Guo along with all members of the group both past and present. I am appreciative of the many collaborators with whom I have been given the privilege to work during my graduate study. This dissertation certainly would not have been possible without the generous support from the David and Lucile Packard Foundation and the Merck Foundation. Most importantly, this milestone would not have been possible without the almighty God who continues to provide for me in ways that are exceedingly and abundantly above all things that I could ever imagine. My wife (Neali) and daughter (London) are two of the greatest examples of his love for me.

## Table of Contents

## LIST OF FIGURES

## LIST OF TABLES

# Chapter 1
# Overview of Nanolithographic Techniques

## Introduction

Fundamental to realizing the full societal impact of current nanoscience research and development efforts are the production of tools that allow for the development of manufacturable systems that translate discoveries to a viable marketplace. The rapid growth of semiconductor technologies over the last 50 years serves as a model for the development of potential nanotechnologies that are primarily connected to the domains of academic research and government laboratories. While fundamental discoveries that are still driving semiconductor innovation occurred many decades ago, the maturation of associated manufacturing processes has allowed these discoveries to produce technologies that have impacted our society in fundamental ways in diverse areas such as healthcare, transportation, communication, and entertainment.

For example, since the manufacturing of the first microprocessor, microchip manufactures have successfully maintained a robust increase in transistor density according to Moore's Law, effectively doubling the transistor density approximately every two years which have ultimate resulted in the proliferation of powerful miniaturized, portable systems such as present-day mobile technologies. While device miniaturization in the semiconductor industry continues to be motivated primarily by tangible benefits of improved device performance and manufacturing costs, the ability of semiconductor device manufacturers to continue to adhere to Moore's Law, and the

associated reduction to subwavelength critical dimensions (CDs), is now threatened by technical challenges and rising cost associated with radiation-based lithographic techniques such as state-of-the art immersion lithography, electron-beam lithography, and the most promising next generation lithography (NGL) approach, ultraviolet lithography (EUV).

The development of strategies within the semiconductor manufacturing industry to pattern structures with smaller CDs that has fueled the sustained evolution of the IC industry has now crossed the sub-100nm threshold that benefits nanoscience research efforts. While resulting discoveries have led to proof-of-concept demonstrations of novel devices. In order to translate these novel devices into commercially viable technologies mirroring the success of the ICs, critical issues related to nanomanufacturing must be adequately addressed. Most notable among the challenges associated with nanomanufacturing are technical barriers related to 3D alignment and assembly of heterogenous systems, high-volume process control, testing, and identification/mitigation of defects

Since its original demonstration in 1995 by Chou et.al, interest in Nanoimprint Lithography (NIL) has grown due to its demonstrated sub-3nm resolution limits and the numerous application areas that have resulted from its versatility. Additionally, it is currently included in 2013 edition of *The International Technology Roadmap for Semiconductors* as a key patterning technique with the potential to be used for high-volume manufacturing (HVM) down to 12nm half-pitch nodes with relatively low cost of ownership (CoO). The dual relevance of NIL to both fundamental research and manufacturing has led to its considerable attention over the last decade as it naturally

positions discoveries for commercial applications. In order to fully appreciate the significance of NIL, it is important to better understand its evolution that has positioned it for impact beyond nanoscience exploration in academic laboratories and into commercial markets.

## Radiation-based Nanopatterning

### Immersion Lithography

Immersion lithography (IL) is a modification to conventional photolithography that increases the numerical aperture (NA) of the exposure system by replacing the air gap between the wafer and lens with a higher refractive index liquid medium (e.g. purified water $n$=1.4). This approach maintains the high-volume manufacturing throughput and leverages existing material/tooling (e.g. mask plates, resist systems) of conventional photolithography. Increasing the resolution further with this technique will require the development of suitable higher index liquid media or the deployment of a shorter wavelength light sources.

### Extreme Ultraviolet Lithography (EUV)

Extreme ultraviolet lithography (EUV) is a leading alternative that will yield resolution enhancements over deep ultraviolet (DUV) lithography systems primarily through the reduction of the exposure wavelength to 13.5 nm. However, there are many challenges that must be addressed to yield a cost of ownership that justifies the adoption of EUV lithography by semiconductor device manufacturers. As with optical lithography, the overall performance of the EUV system will depend on the ability to

adequately address issues related to the key components which include the light source, imaging elements, resists and masks.

The production of a suitable light source is required to achieve sufficient wafer throughput. This issue of limited source power is being compensated through the development of new resist formulations with increased sensitivity at 13.5nm. Due to material absorption at this wavelength, refractive optics (i.e. lenses) are incompatible and multilayer mirrors (MLMs) composed of Mo-Si stacks must be utilized.

**Fundamentals of Nanoimprint Lithography**

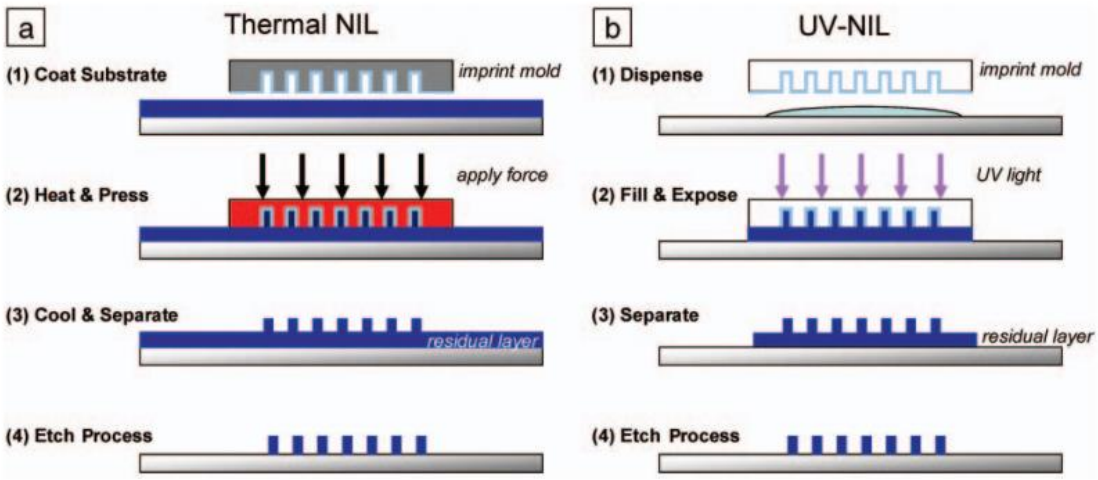


**Figure 1.1 Schematic of the standard NIL process consisting of the mechanical pressing of a hard mold into thermoplastic polymer coated substrate. RIE is used to remove the residual polymer layer[1]**

The original thermal nanoimprint lithography (T-NIL) process involved the creation of surface relief patterns in a polymeric resist using hard silicon master molds in a hot embossing process. Further NIL development resulted in ultraviolet nanoimprint lithography (UV-NIL) where a low-viscosity UV-curable polymer precursor is used as

the resist. As illustrated in Figure 1.1, the general NIL process involves the application of a thermoplastic or UV-curable polymer resist—commonly using spincoating—on a suitable substrate. The mechanics of the subsequent steps highlight the different attributes of T-NIL and UV-NIL.

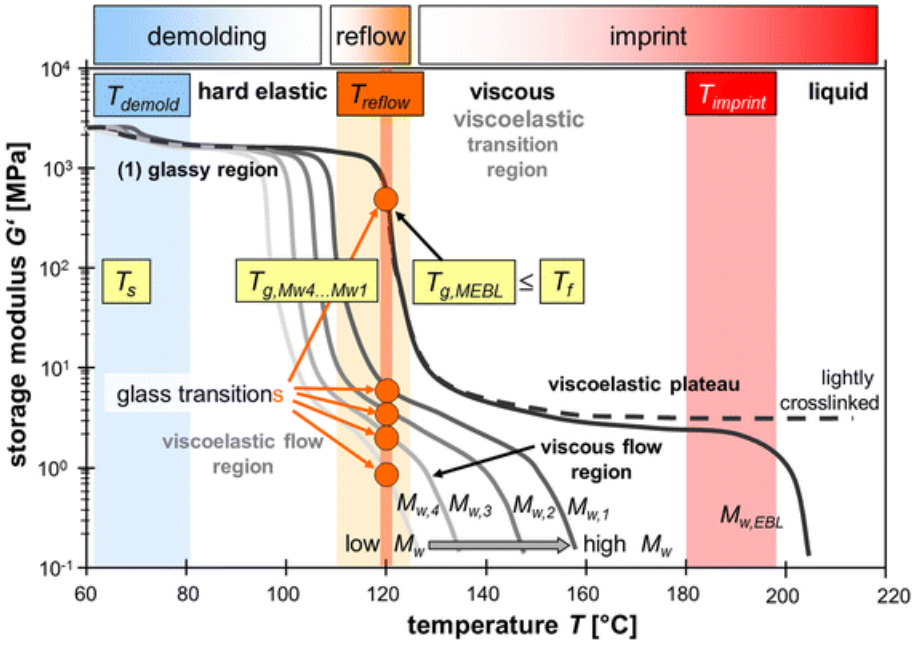


**Figure 1.2-Schematic showing the changes in mechanical properties of a polymer possessing a *Tg* of 100 °C[2].**

In T-NIL, the mold containing nanoscale patterns is placed in contact with the substrate and the temperature of the mold-substrate assembly is increased to approximately 50-80 °C above the glass transition temperature ($T_g$) of the particular nanoimprint resist—within a viscous flow regime--prior to application of pressure to create conformal contact between the mold and nanoimprint resist. The change in the polymer viscoelastic properties with temperature is illustrated in Figure 1.2. Below $T_g$ the polymer is considered a hard elastic, glassy material. Note the elasticity of the material drops significantly around $T_g$ which has been demonstrated to vary from bulk values when using thinfilms and also influenced by the underlying substrate. Further

increase above the $T_g$ eventually causes the thermoplastic resist to pass through the viscoelastic region and into the viscous flow region which is ideal for the imprint process. The threshold temperature for viscous flow of the polymer is dependent on the molecular weight ($M_w$) of the polymer, with higher $M_w$ polymers requiring higher temperature. This can be viewed as a consequence of the increased interaction between polymer chains that are longer and/or more highly cross-linked or branched.

After cooling the mold-substrate assembly well below $T_g$, the mold and sample are separated, leaving behind a replica of the nanopatterns of the mold within the thermoplastic resist. Depending on the targeted application, it is often necessary to use the resist pattern as a mask for further transfer to the underlying substrate material (e.g. Si, $SiO_2$). In this case, a short dry etch using oxygen plasma is required to remove a residual layer of nanoimprint resist and expose the underlying substrate. The required thickness of the spincoated nanoimprint resist is determined by the specific nanostructures contained within the mold and the resulting residual layer helps to protect the nanopatterned structures of the mold during the imprint process by behaving as a soft cushion. In order to maintain that fidelity of the pattern transfer, it is important to minimize the thickness of the residual layer in order to minimize the required duration of the isotropic oxygen plasma etch.

**Defectivity**

Reduction of defectivity to less than $1cm^{-2}$ is a challenge that must be met prior to adoption of NIL as HVM technique. Replica defects can be associated with defects contained within the original 1x master, particulates, incomplete cavity filling due to air pockets, or plugs due to pattern damage during demolding. The use of filtered resist has

led to improvements in defectivity. Additionally, wafer bowing technique that allows the resist to move outward from the center of wafer outward has reduced the probability of air trapping and incomplete filling. Moreover, due to polymer rheology, imprint defects are more likely to occur in areas there is a transition in pattern characteristics (i.e. density, depth etch, width). The use of a resist formulation possessing sufficient mechanical strength after completion of the imprint, crosslinking/cooling, and demolding is critical.

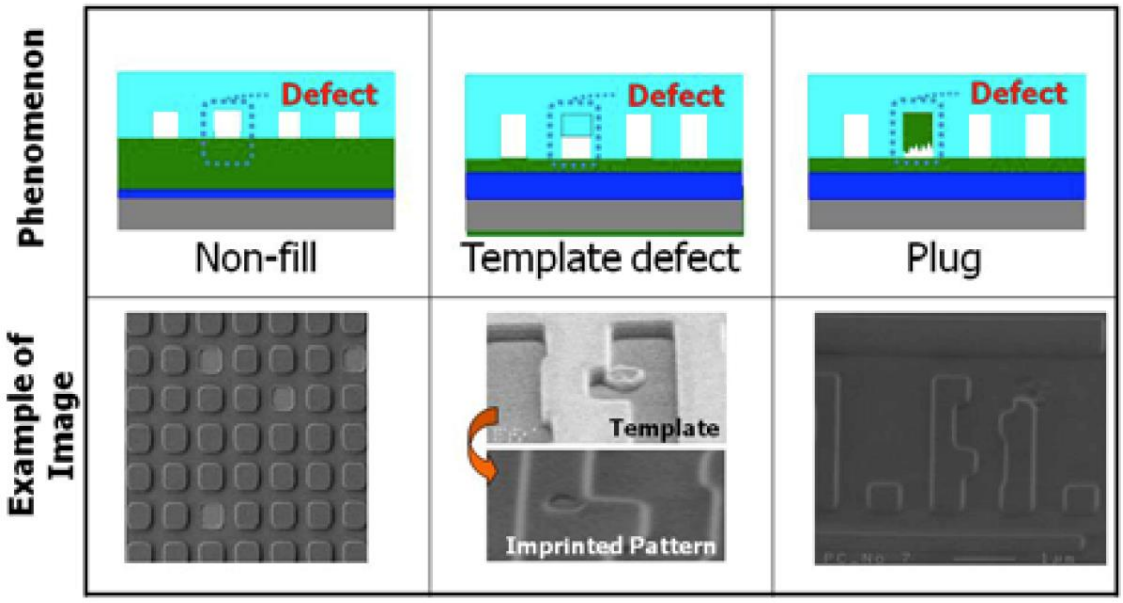


**Figure 1.3 Example of defects resulting from nanoimprint [3]**

## Mold Template Generation

Critical to the development of NIL are the techniques available to produce the initial mold surface relief patterns. As NIL is a conformal 1x technique, the defect density found in the mold sets the upper limit on the quality of the patterns and performance of resulting devices. Given the propagating impact on the subsequent

fabrication steps, methods to produce high-quality molds have received considerable attention.

Key considerations when selecting a method to produce a mold of sufficient quality are pattern density and critical dimensions, overlay requirements, thermal expansion compatibility between mold and substrate for T-NIL, and mold and/or substrate transparency for UV-NIL. Since NIL is a mechanical molding process, materials possessing sufficient hardness (i.e. high Young's modulus) must be utilized. For the traditional imprinting of thermoplastic polymer resist systems, previous works have demonstrated success using molds composed of metals (e.g. Ni), Si, and dielectrics such as silicon, silicon nitride and alumina. Relevant properties of a few demonstrated mold materials are listed in Table 1.1.

| **Material** | **Thermal expansion ($10^{-6}K^{-1}$)** | **Elastic Modulus (GPa)** | **Poisson's ratio** |
|---|---|---|---|
| Silicon | 2.6 | 131 | 0.28 |
| Silicon Dioxide | 0.6 | 73 | 0.17 |
| Silicon Nitride | 3.0 | 215 | 0.27 |
| Aluminum Oxide | 35 | 375 | 0.22 |
| Nickel | 13.4 | 200 | 0.31 |
| PDMS | 310 | 0.0006 | 0.5 |

**Table 1.1 Relevant properties of a few demonstrated mold materials[4].**

The hardness requirement will depend heavily on the specific attributes of the pattern (e.g. pattern density, minimum lateral dimensions of constituent structures, and

pattern depth). Taller nanostructures with lower pattern density will require molds possessing higher mechanical strength. In order to leverage the high-throughput attribute of NIL, molds should be sufficient robust and able to withstand the stress associated with high-frequency pattern replication.

The basic approach to producing a mold involves a suitable lithographic technique to generate the initial patterns followed by the deposition of a masking material used for reactive-ion etching (e.g. Cr, Ni) the desired pattern into the underlying substrate and lift-off. If NIL is used as the patterning technique, it is important to note the potential impact of using a thermoplastic polymer resist system on a different substrate material. Since thermoplastic imprinting requires significant ramps in temperature around $T_g$, pattern distortions can be generated due thermal mismatch between mold and substrate materials which result in significant stress within the pattern polymer film.

Advances in NIL polymer resist systems compelled the production of soft, flexible molds and that improve the fidelity of pattern transfer has also been demonstrated. As NIL is a conformal patterning process, adding more flexibility to the mold allows for more intimate contact with the polymer resist and minimizes the defect area associated defects occurring in the original mold or resulting from particulates present during the replication process. Initial efforts in this regards focused on the use of mold possessing a hard bulk substrate material with a thin flexible regioflex patterned surface.

The surface energy of the mold material must also be considered when developing a process flow that utilizes NIL. Mold-sample separation is the final step of the imprint process and must be accomplished reliably. If the surface energy of the mold is not

adequately produced, it will cause pattern degradation due to sticking of the imprint resist to the mold. One approach to address this issue is to produce a mold from a low-surface energy material. Another proven approach is to fluorinate the surface of the mold using a surfactant such as perfluorodecyl-trichlorosilane using either a vapor-phase or solution-phase approach. The higher the pattern density of the mold, the greater the interfacial area between the mold and polymer resist making the use of a surfactant release agent more critical to the success of the imprint process.

**NIL Derivatives**

Further development of NIL has led to the maturation of variants such as UV-Nanoimprint Lithography (UV-NIL), Step and Flash Imprint Lithography (S-FIL), micro-contact printing and roll-to-roll imprinting. The most significant difference of UV-NIL versus standard NIL is the use of a low-viscosity, UV-curable resin as the nanoimprint resist as opposed to a thermoplastic polymer. By transferring the pattern from a mold to a low-viscosity resist, throughput is significantly increased over the traditional NIL approach as the resist conforms to the mold patterns as a result of capillary action.

The successful development of UV-NIL and its required resist systems has led to its demonstration as a means for high-fidelity, full-wafer pattern transfer. Building from the foundation laid by NIL and UV-NIL, S-FIL has been demonstrated as a viable technique that can further increase throughput of the NIL process. Similar to the cost impact of step-and-flash lithographic patterning techniques which reduces the constraints of the original mask pattern, S-FIL involves the repeated imprint and relative mold-sample displacement to pattern larger areas using smaller molds.

**Thesis organization**

This thesis extends the relevance of NIL by demonstrating its impact on applications related to biotechnology, photonics, and energy conversion devices. Work reported in this thesis has previously been published in [5-8]. Chapters 2 demonstrates the application of NIL to the field of plasmonics. Chapter 3 compares the plasmonic response between NPAs fabricated with the methodology outlined in Chapter 2 and thermally annealed metal films. Chapter 4 explores the use of NIL-produced plasmonic arrays for biosensing. Chapter 5 demonstrates the ability of NIL to enhance the performance of microfuel cells. Chapter 6 summarizes findings and highlights a few opportunities to extend the work of this thesis.

## References


[1] M. D. Stewart and C. G. Willson, "Imprint materials for nanoscale devices," *Mrs Bulletin,* vol. 30, pp. 947-951, Dec 2005.

[2] H. Schift, "Nanoimprint lithography: An old story in modern times? A review," *Journal of Vacuum Science & Technology B,* vol. 26, pp. 458-480, 2008.

[3] T. Higashiki, T. Nakasugi, and I. Yoneda, "Nanoimprint Lithography for Semiconductor Devices and Future Patterning Innovation," *Alternative Lithographic Technologies Iii,* vol. 7970, 2011.

[4] L. J. Guo, "Recent progress in nanoimprint technology and its applications," *Journal of Physics D: Applied Physics,* vol. 37, pp. R123-R141, 2004.

[5] A. D. Taylor, B. D. Lucas, L. J. Guo, and L. T. Thompson, "Nanoimprinted electrodes for micro-fuel cell applications," *Journal of Power Sources,* vol. 171, pp. 218-223, 2007.

[6] B. D. Lucas, J.-S. Kim, C. Chin, and L. J. Guo, "Nanoimprint Lithography Based Approach for the Fabrication of Large-Area, Uniformly-Oriented Plasmonic Arrays," *Advanced Materials,* vol. 20, pp. 1129-1134, 2008.

[7] A. M. Lopatynskyi, V. K. Lytvyn, V. I. Nazarenko, L. J. Guo, B. D. Lucas, and V. I. Chegel, "Au nanostructure arrays for plasmonic applications: annealed island films versus nanoimprint lithography," *Nanoscale research letters,* vol. 10, pp. 1-9, 2015.

[8] V. Chegel, B. Lucas, J. Guo, A. Lopatynskyi, O. Lopatynska, and L. Poperenko, "Detection of biomolecules using optoelectronic biosensor based on localized surface plasmon resonance. Nanoimprint lithography approach," *Semiconductor Physics, Quantum Electronics & Optoelectronics,* vol. 12, pp. 91-97, 2009.

# Chapter 2
# Plasmonic Nanoblock Arrays Fabricated Via Nanoimprint Lithography

## Introduction

Plasmonics has experienced tremendous growth over the two last decades due to the maturation of methods to produce metallic thinfilms and nanoparticle constructs. The relevance of nanoimprint lithography (NIL) to this growing field is demonstrated in this chapter via the fabrication of metallic nanoparticle arrays (NPAs) using a grating-based double imprint scheme. The resonant excitation of surface plasmons (SPs), quanta of electron density oscillations found at metal-dielectric interfaces, is referred to as surface plasmon resonance (SPR) for planar interfaces and localized surface plasmon resonance (LSPR) for nanostructured interfaces. The characteristics of these surface electromagnetic waves have received considerable attention due to their potential impact on photonic and optoeletronic systems.

## Surface Plasmons

Theoretical inquiries of SPR were initiated in the 1950s by Ritchie et.al. who predicted the presence of a surface-dependent resonant mode when probing metallic thinfilms using low-energy electrons beams. Over the next quarter-century, numerous experimental investigations using electron loss spectroscopy yielded greater details about the characteristics of the SPs. With the growing theoretical understanding of SPs,

numerous experimental studies began looking at ways to leverage the associated resonant phenomenon to enhance low yield spectroscopic methods such as Raman spectroscopy.

The development of nanoparticle synthesis methods over the last decade has generated an increased research focus on localized surface plasmons. In a similar manner to the fundamental study of SPs and development of SPR-based systems, LSPR appears to be following a similar arc of discovery. In order to fully appreciate the context of this current work regarding LSPR, it is prudent to first highlight key characteristics and applications related to SPR.

For example, the ability to couple SPR modes and free-space light presents an opportunity to produce high-speed microchips with optical interconnects which will eliminate speed limitations imposed by resistive-capacitive (RC) delays found in integrated circuits. This type of optoelectronic system would require a method to convert between electronic signals and SPR modes and is considered a promising approach based on work reported by Brogersma et.al [9]. Another notable application area for SPR is in the field of biotechnology where the coupling of light into SPR modes of metallic thinfilms is used as a transduction mechanism in biosensor systems. In order to better understand SPR relevance to these photonic systems, it is important to understand the basic physics underlying this phenomenon and the associated technological constraints which can be elucidated by examining the properties of a basic metal-dielectric interfacial system.

Through the application of electromagnetic theory to a single metal-dielectric interface, it is found that SPs possess the following characteristics:

(1) SPs exist only for TM polarization;

(2) The resonant condition for coupling light into SPs is influenced by the dielectric refractive index and bulk plasmon frequency $\omega_p$ of the metal; and

(3) Excitation of SPs with free-space light at a planar metal-dielectric interface requires a suitable coupling mechanism for phase matching based on the dispersion relation.

Interfaces consisting of metals with higher electron densities produce SPs at shorter excitation wavelengths. Moreover, it is important to note that SP damping, and therefore the associated propagation length, depend on the collision rate of conduction electrons and interband transitions of valence electrons within the particular metal. SP propagation lengths are connected to the specific attributes of the mode confinement. Modes possessing larger penetration depths and confinement within the metal film result in more loss and shorter propagation distances. Table 2.1 shows a comparison of the key SP characteristics for silver and gold films.

| **Metal layer supporting SPW** | **Silver** | **Gold** |
|---|---|---|
| Propagation length (μm) | 19 | 3 |
| Penetration depth into metal (nm) | 24 | 29 |
| Penetration depth into dielectric (nm) | 219 | 162 |
| Concentration of field in dielectric (%) | 90 | 85 |

**Table 2.1--SP characteristics for a metal-water interface at 630nm Adapted from [10]**

**Localized Surface Plasmons and Nanoparticle Synthesis**

Localized surface plasmon resonance (LSPR), collective electron density oscillations found in noble metal nanostructures, has been studied extensively over the past decade due to its potential utility as the backbone for a number of photonic technologies capable of controlling light at nanoscopic dimensions well below the diffraction limit [11, 12]. Research in this field has been engendered by the tremendous growth in fabrication methods capable of producing an enormous variety of nanoparticle (NP) systems and nanostructured films.

Numerous theoretical and experimental studies have established that LSPR is sensitive to the shape, size, interparticle distance, dielectric environment and material composition of the constituent NPs[13-16]. Additionally, optical dichroism observed from well-aligned nanoparticle arrays has demonstrated the polarization dependence of their LSPR response[17-19]. One of the most promising applications of nanoparticle systems is their use as real-time chemical and biological sensors that originate from the aforementioned LSPR dependence on their dielectric environment. Such systems have been demonstrated using a variety of NP implementations including single-particle, one-dimensional and two-dimensional array configurations on transparent substrates as well as solution-based methods[20, 21].

An abundance of nanofabrication techniques have been employed to produce the desired nanostructures utilized in LSPR studies with varied degrees of success as measured by parameters such as monodispersity. A few examples of these techniques include electron beam lithography, templates, nanosphere lithography (NSL) and colloidal solution-based nanoparticle synthesis—of which the latter two have been used

quite extensively [14, 22-24]. Although NSL and solution-based methods have been effective for fundamental studies of the influence of NP characteristics on LSPR, there are still significant limitations of both techniques that limit their applicability for LSPR-based applications.

Chemical synthesis techniques have the advantage of creating a wide array of exotic nanostructures based on modification of the reaction parameters such as time, relative concentration of reactants and temperature. However, the monodispersity and reproducibility of desired structures can be difficult to achieve using this method. More importantly, this technique lacks the control of relative NP positioning and orientation in addition to the requirement of novel surface chemistries for the reduction of NP agglomeration and effective substrate attachment. The inability to precisely control the sample-to-sample LSPR response of immobilized NP systems is a severe limitation of this fabrication approach.

Nanosphere lithography is an alternative fabrication method introduced by Hulteen et. al. to produce periodic particle arrays (PPAs) directly on a variety of substrates. This technique utilizes a closed-packed nanosphere mask that permits direct deposition of noble metal NPs onto a substrate through the interstitial regions of the mask. NSL has been implemented in a single-layer and double-layer approach with extensive characterization and utilization of triangular nanoparticles resulting from the single-layer method. The precise control of PPA attributes afforded by this technique makes it a promising candidate as a fabrication method relevant to commercialized LSPR applications. Limitations of NSL include issues with surface coverage and the geometric constraints imposed by the nanosphere mask on the PPA lattice structure and NP shape

characteristics which reduce the degrees-of-freedom available for the designed LSPR response of the PPA system.

In order to address and supplement limitations encountered by a number of current NP fabrication methods, we propose the use of Nanoimprint Lithography (NIL) and two-dimensional nanostructure array (*nanoblock*) molds derived from one-dimensional gratings to produce noble metal NPAs. We believe this approach possesses a number of attributes that will not only enhance the fundamental study of NP systems, but may also play a key role in the production of marketable LSPR technologies. First, NIL is a mold-based, high-throughput and low-cost process capable of patterning large areas with sub-10 nm resolution capable[25, 26]. Second, the benefits of alternative nanofabrication methods capable of creating unique LSPR nanostructures and possessing less desirable throughput and cost characteristics can be maximized through their use for creation of NIL molds that enable the perpetual reproduction of these structures. This characteristic of NIL to "preserve" nanostructures in a mold permits the optimization of NPAs for particular LSPR applications through empiricism. Moreover, the use of one-dimensional grating structures as the foundation to create NPAs enables resulting two-dimensional patterns of varying complexity to be geometrically interpreted and modelled for design purposes.

In this chapter, we explore a NIL fabrication approach capable of creating uniformly oriented and homogenous noble metal NPAs. Extensions of this fabrication method demonstrating the flexibility of this technique to produce NPAs possessing a variety of unique structural and LSPR characteristics are discussed. In order to further elucidate the utility of this technique, the LSPR dependence of NPAs composed of rectangular

constituent NPs on various attributes including polarization, composition, height, aspect ratio and dielectric embedding media are experimentally ascertained.

## Methods

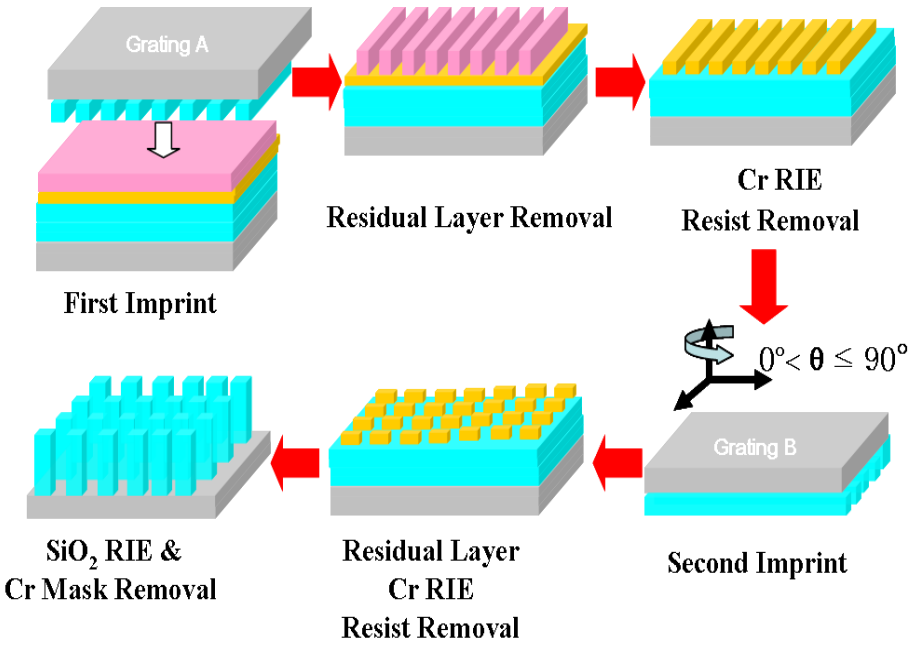


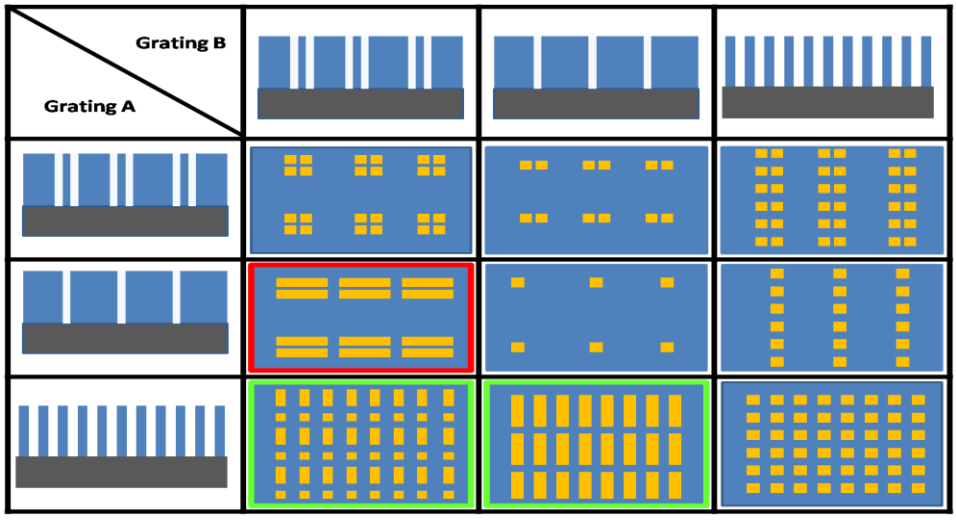


**Figure 2.1 (Top)Illustration of the general process used to fabricate "nanoblock" molds possessing different lattice and particle geometries.(Bottom) Matrix illustrating possible nanoparticle array configurations from A90B nanoblock molds produced using a collection of one-dimensional grating molds with different profiles. The red bordered array is produced using the inverse profile of grating A. Similarly, the green bordered arrays are achieved using the inverse of grating B.**

Illustrated in Figure 2.1 is the general approach used to create large-area molds that are subsequently used to fabricate NPAs. First, a suitable substrate is coated with a mask layer and spincoated with nanoimprint resist. The resist is patterned using a one-dimensional grating mold (A) and the pattern is transferred to the underlying mask layer (e.g. Cr) through a suitable etching process. After removing the previously patterned resist, a new layer of resist is applied for a second imprint with a one-dimensional grating mold (B) rotated θ relative to the previous imprint. The pattern is again transferred to the underlying mask layer by an etch process resulting in a two-dimensionally patterned mask layer that is subsequently used to produce a two-dimensional array of "nanoblocks" in the substrate material through a suitable anisotropic etch process. Large-area metallic NPAs are produced by these nanoblock molds through conventional NIL processing steps consisting of imprinting, residual polymer removal, metallization and lift-off.

This technique is extremely powerful in creating a variety of structures by simply using one-dimensional gratings with differences in their lateral characteristics (i.e. duty cycle or period) and relative angular orientation $\theta$ for successive imprints. Benefiting this technique are the numerous realized methods used to produce, modify and optimize one-dimensional grating structures[25, 27-30].

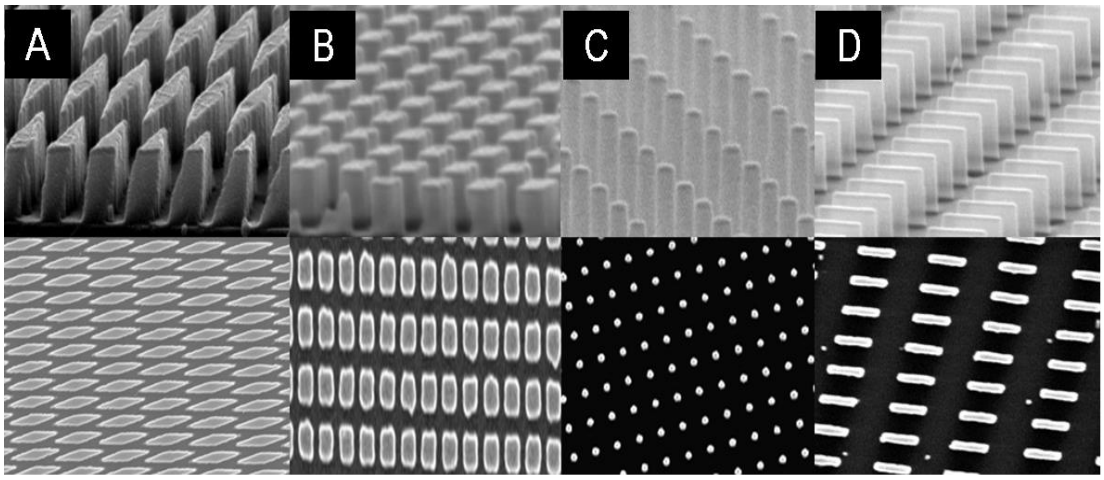


**Figure 2.2 SEMs of representative nanoblock molds derived from one-dimensional gratings**

For example, if the same grating mold is used and oriented orthogonally for successive imprints (A90A), a square lattice of rectangular or cylindrical (due to the reduced anisotropy of the etching process*)* nanoblocks (Figure 2.2 B and C) are realized. However, if this same process is repeated with a non-orthogonal orientation for successive imprints such as $\theta$=45°, an array of diamond nanoblocks is produced on a rhomboidal lattice (Figure2.2 A). Likewise, if two different grating structures are utilized in a AθB scheme, it is possible to create two-dimensional lattices of rectangular (θ =90, Figure 2.2 D) and diamond nanoblocks (90>θ>0). Consequently three unique NPAs (AθA, AθB, BθB) are possible by simply using a combination of two different grating structures at one particular relative orientation $\theta$.

NPAs with interparticle distances that allow them to behave effectively as single NPs or highly coupled NP systems are possible by combining gratings with the appropriate line density. For example, a large area of one-dimensional NP chains in different structural formats (e.g. single particle, dimers, etc.) are feasible using low and high line density gratings in an A90B scheme with single period or multi-period one-

dimensional gratings. Similar structures have demonstrated narrow plasmon peaks and excellent potential LSPR sensing capabilities[31]. Likewise, effectively isolated NPs are possible by combining two low-density gratings.

The flexibility and utility of this fabrication approach is further highlighted by the numerous studies resulting from nanostructures derivable by this technique. A great deal of interest in nanostructured thinfilms currently exists due to their surface plasmon-enhanced transmission properties and potential applications [32]. These nanopatterned films are accessible using this technique by simply creating the negative of the nanoblock molds and employing conventional NIL or using a previously demonstrated negative-tone NIL process (n-NIL) [33] . NSL produced nanowell structures have been demonstrated by Hicks et. al. to produce narrow LSPR peaks and enhanced sensitivity to dielectric changes [34]. These structures are achievable using our NIL-based technique by imprinting with a NPA mold of the proper depth and using the appropriate metallization. The use of NIL inherently increases throughput and reduces the cost associated with producing such a structure in addition to simplifying the fabrication through the elimination of RIE. As over ten billion nanoparticles are created using a nanoblock mold derived from 200nm period gratings covering an area of $1cm^2$, NPs can be massively produced, functionalized and released from their substrate for use in a solution-phase detection scheme [35].

**Nanoblock Mold Fabrication**

A thin 10nm film of Cr serving as the mask layer was electron beam evaporated on 200nm thermally grown $SiO_2$. The nanoimprint resist (MicroResist MR- i-8020; $T_g$=115 °C) was spincoated on the substrate to the appropriate thickness (determined by

mold depth, duty cycle and period), baked on hotplate (140 °C; 5 min) to remove residual solvent and imprinted in a custom-built nanoimprinter (670 psi; 5 min.; 180 °C). After separation of the mold and substrate, the residual polymer was removed in an $O_2$ plasma and the pattern was transferred to the Cr layer using RIE (40/8 sccm $Cl_2/O_2$; 200 W; 150 mT). The resist was stripped using an Acetone soak, rinsed with Methanol and IPA and dried using $N_2$. The above process steps were repeated for the second imprint with the grating direction rotated relative to the first imprint. The 200 nm $SiO_2$ was subsequently reactive-ion etched *(*20 sccm $CHF_3$; 20 mT; 150 W) using the patterned Cr mask. After etching, the Cr mask was removed using a wet chromium etchant (CR-14; Cyantek Co.), rinsed with a copious amount of deionized water (DI:$H_20$) and dried with $N_2$. The mold was then prepared for imprinting by vapor-phase surfactant treatment to reduce mold-polymer adhesion.

**NIL Sample Fabrication**

Pyrex glass substrates were cleaned in a 1:1 pirhanna solution (30% $H_2O_2$: 29% $NH_4OH$), rinsed with a copious amount of DI:$H_20$ and dried using $N_2$. The resist was spincoated to the appropriate thickness on the substrate, baked on a hotplate for solvent removal and imprinted. After separation, the residual polymer layer was removed using $O_2$ plasma reactive-ion etching. Metallization was accomplished using an electron beam evaporator by first depositing a 1-3 nm Ti adhesion layer followed by the mass thickness of Au or Ag as determined by the in-situ monitoring system. Liftoff was performed by soaking the sample in Acetone inside of a low-power ultrasonic bath. After completion of lift-off, samples were rinsed with methanol and IPA and dried with $N_2$.

**E-beam Lithography**

Coverglass was first cleaned with a piranha solution (1:1 $H_2SO_4$:$H_20_2$) for 30 minutes. They were then rinsed copious amounts of DI water for 5 minutes and dried using $N_2$. A2-Poly-methyl Methacrylate (Microchem) was chosen as the resist and was spincoated to a thickness of ~100nm. After baking on a hotplate (10 min, 110 °C) a thin 10 nm layer of Al was deposited in order to minimize substrate charging during ebeam exposure (Raith 150, 5 kV, nominal dose = 0.01 fC). A dose matrix for each structure was performed in order to determine the appropriate range of exposures for the various patterns.

**Nanoparticle Array Optical Characterization**

Extinction measurements were acquired using a Nikon TE300 Eclipse inverted microscope (20x objective; *NA*=0.44) with transmitted light coupled into an Ocean Optics fiber-coupled spectrometer (HR-4000 or SD-2000) using an achromatic lens. For polarization dependent extinction measurements, a linear polarizer mounted in a rotating module was aligned to the optic-axis of the microscope directly above the sample stage. All measurements were taken using normally incident light and unpatterned was used as a reference.

Darkfield microspectroscopy was implemented using a Zeiss Axiovert 200 inverted microscope. An oil immersion ultra-darkfield condenser (*NA*=1.2-1.4) and a 100x oil immersion Plan-neofluar® (Zeiss) objective (adjustable numerical aperture, from 0.7 to 1.3). Illumination was provided by an integrated 100 W halogen source. A selectable output adapter is connected to the microscope camera port that allows the

sample image to be directed to either a color digital camera or a line-imaging spectrometer. The imaging camera was a Photometrics CoolSnap CF which is used to record the field of view for co-registration with the spectrometer (Acton Research SpectraPro 2150i).

**Modification of Dielectric Environment**

Bulk refractive changes were introduced by flowing glycerol/DI:$H_20$ mixtures of different relative concentrations ($n$=1.33-144) through a custom-built flowcell. Refractive indices of the mixtures were determined using a refractometer (Fisher Scientific). Electron beam evaporation of silicon oxide ($SiO_2$) was used to create distance dependent changes to the surrounding refractive index profile.

**Surface Enhanced Raman Spectra**

Measurements were performed on a commercially available Raman microscope (Renishaw inVia Reflex) using neat 1-Phenyloctane (Acros Organics). He-Ne ($\lambda$= 633 nm) laser was used as the excitation source. Pyrex glass containing Ag square NPA (height=20 nm) was used as the substrate and referenced to a planar Ag film.

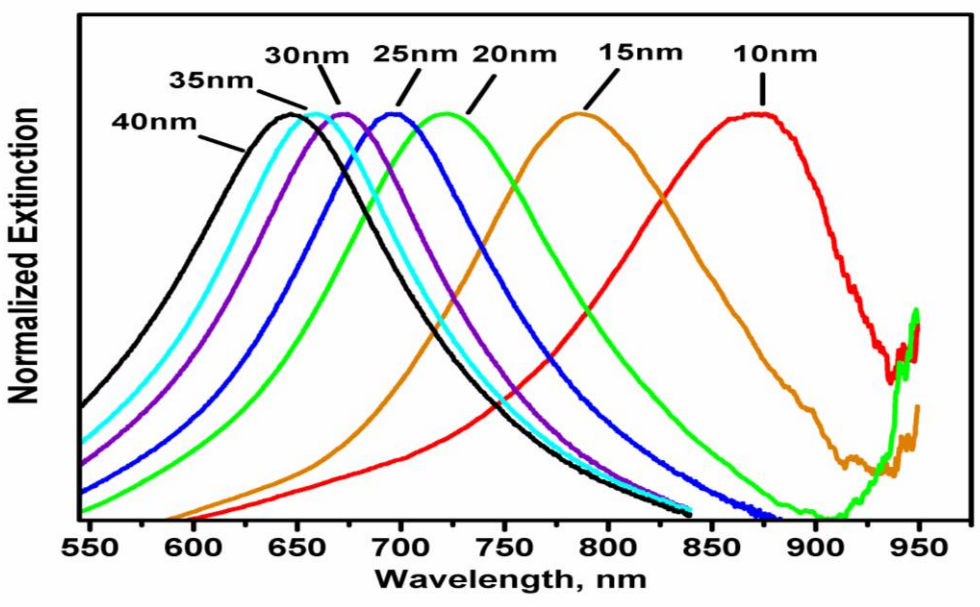


**Figure 2.3 Au square NPA (1nm Ti adhesion layer) with varying nanostructure height demonstrating the inverse relationship between NP height and LSPR peak wavelength.**

## Results

### Height Dependence

An ideal method to produce LSPR nanostructures would permit the optimization of their response for a specific application such as surface enhanced Raman spectroscopy (SERS) where it has been previously shown that the electromagnetic enhancement of specific Raman bands are influenced by their relative position to the LSPR of the substrate. This tunability aspect is demonstrated in Figure 2.3 for Au NPAs only differing in their nanostructure height. A blue shift in the LSPR of the NPAs for both Au and Ag was found to occur for increasing height of the nanostructures. Readily apparent from this data is the nonlinearity of wavelength shift as a function of nanoparticle height. We believe that this can be attributed to the influence of the increasing proximity of the

LSPR to a wavelength region where additional material dependent resonances characteristic of Au (e.g. interband transitions) occur.

Figure 2.4 shows the influence of NP height on the aforementioned dichroic properties of the NPAs. Similar to the effect of height on the resonant wavelength for unpolarized excitation, NP height is inversely proportional to the peak wavelength differential defined as the difference between resonant wavelengths of the longitudinal and transverse modes.

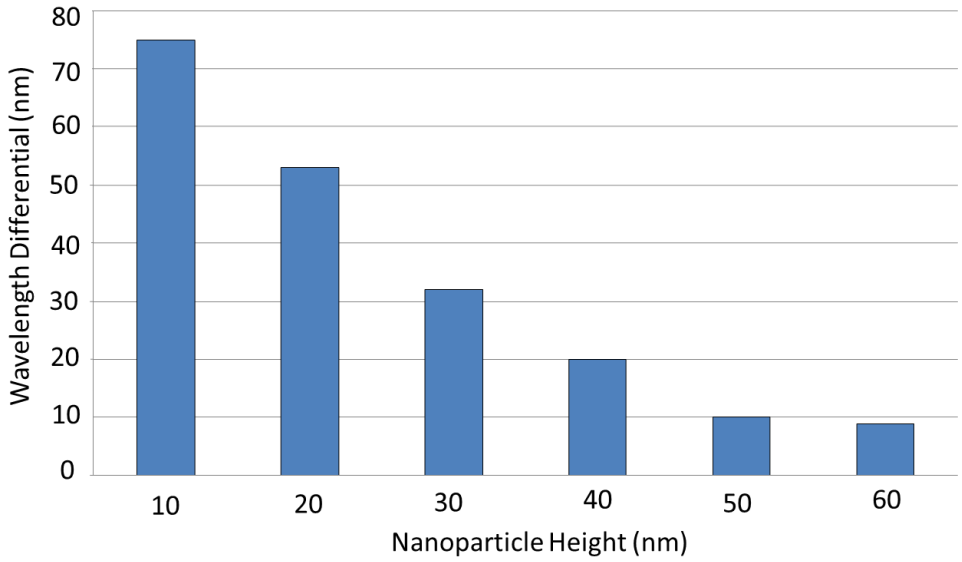


**Figure 2.4 Influence of nanoparticle height on the dichroic behavior for NPAs (period=200nm, short-axis=115nm, long-axis=120nm). Wavelength differential between the peaks associated with long-axis and short-axis polarization decreases with increasing NP height.**

## Effect of Ti Adhesion Layer

The sensitivity of the NP plasmonic response to the dielectric surrounding allows the use of different substrates to manipulate the LSPR condition for surface-confined NPs. To improve the adhesion of NPs to various substrates, thin adhesion promoting layers (<5 nm) of materials such as Ti and Cr are often utilized. Given the established

LSPR dependence on refractive index of materials surrounding NPs, it is important to ascertain the extent to which the adhesion layer contributes to the overall plasmonic response. Figure 2.5 shows the influence of a thin Ti underlayer on the plasmonic response of a nanoblock array. Ag and Au are similarly impacted by the Ti underlayer with the addition of the Ti underlayer resulting in a redshift of the LSPR wavelength relative to NPs deposited directly on a bare substrate. Additionally, 1nm of Ti minimizes the FWHM. It was found that a further increase of the Ti adhesion layer drastically reduced the Q of the resonance and led to an increase in the FWHM.

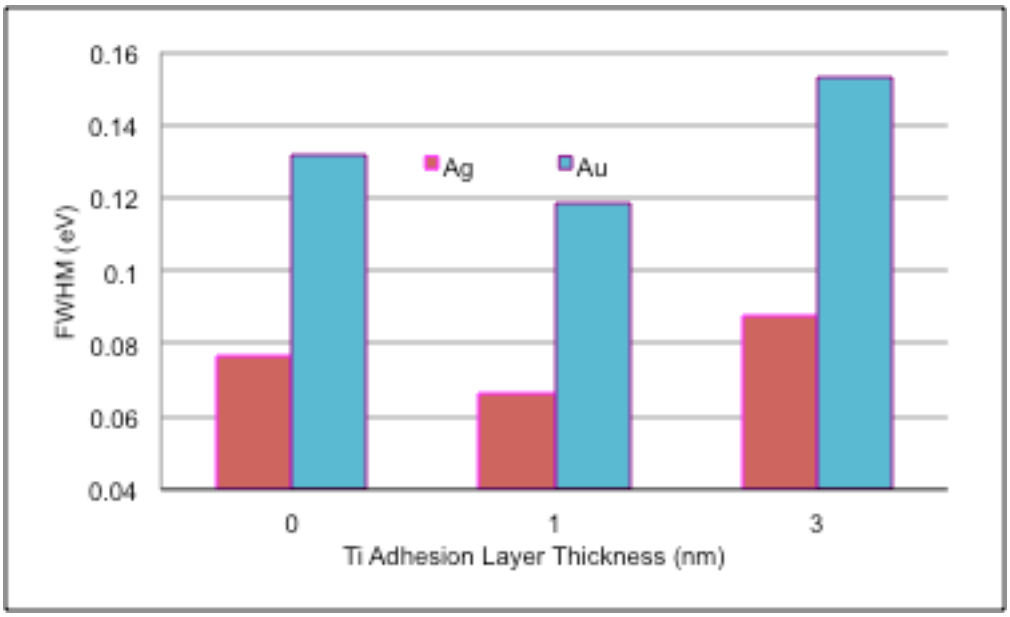


**Figure 2.5 LSPR dipolar peak full-width at half-maximum (FWHM) for 200nm period Au and Ag NPAs (height=20nm). 1nm Ti adhesion layer was found to minimize the FWHM.**

## Material Composition

Changing the material composition of the constituent nanostructures from Au to Ag yields a resonance that occurs more towards the center of the visible spectrum (Figure 2.6). As a result of this material dependence, the difference in optical properties for nanostructures differing in height by 10 nm is clearly observed through their pronounced difference in color. Similar to the case for Au, the resonance is more blue-shifted for the

taller nanostructures. The significant increase in extinction occurring between 10 nm and 20 nm height can be attributed to damping due to increased surface scattering of electrons with longer mean-free paths. Additionally, the strength of our large-area fabrication approach is manifested through the ability to fabricate sample areas possessing different resonances and colors on one substrate (Figure 2.6)

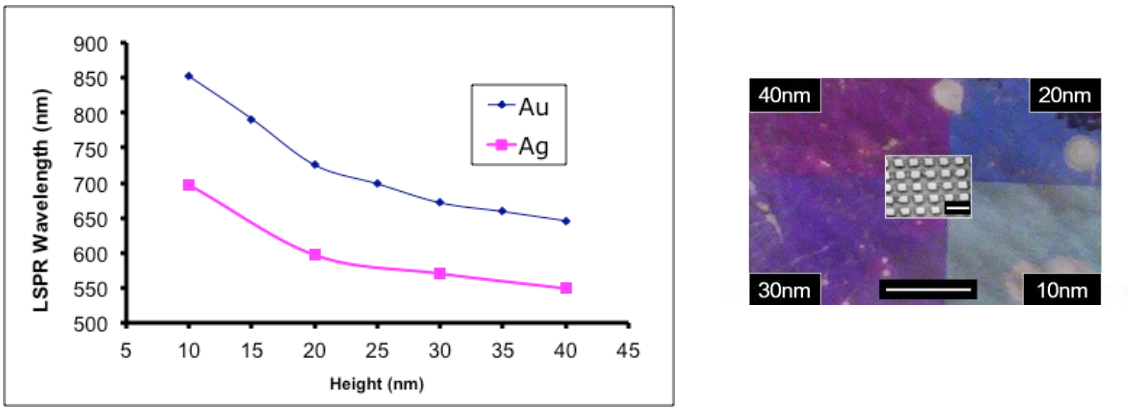


**Figure 2.6 LSPR wavelength dependence on height for Au and Ag NPAs (right) Image of Ag NPA (inset:representative SEM) samples containing quadrants of different heights. scale bar=5mm**

## Bulk Refractive Index Sensitivity

One of the most promising applications of noble metal NPAs is LSPR-based sensing. In order to demonstrate the ability of the NIL-produced NPAs to transduce changes in the local dielectric environment through their LSPR response, the dielectric sensitivity ($\Delta\lambda/\Delta n$) as a function of height was determined (Fig. 2.7). NPs possessing a smaller out-of-plane height yield a higher dielectric sensitivity as determined by the slope of the best-fit line. Additionally, it was also found that Ag NPAs of the same height are more sensitive than their Au counterparts. These findings correlate well with previous

reports using NSL-derivedNPAs[36].

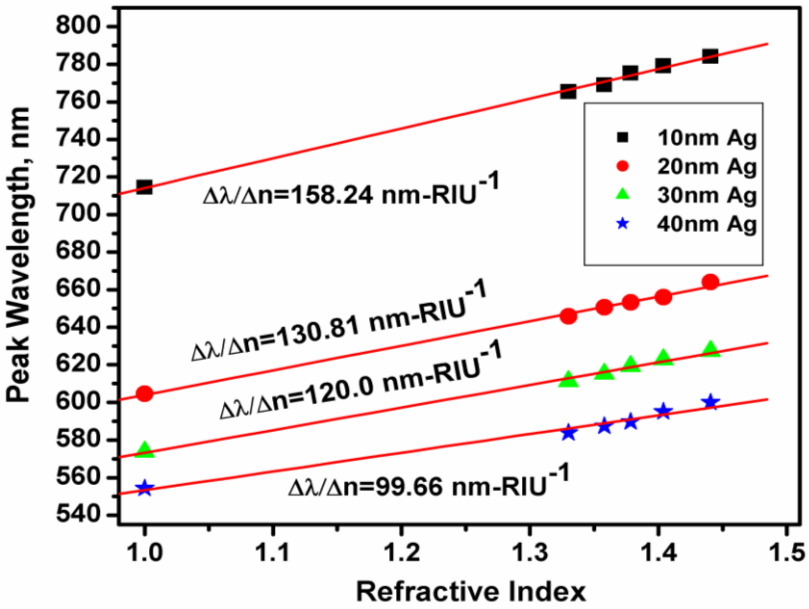


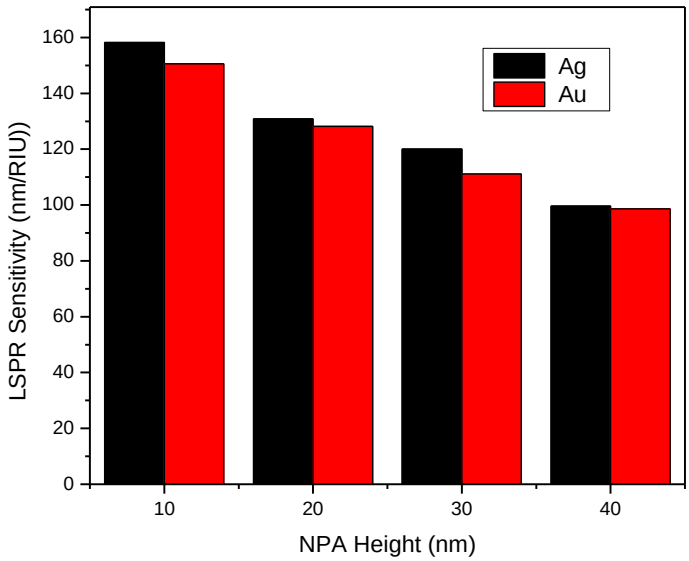


**Figure 2.7 (Top) Extinction peak wavelength as a function of the refractive index of the embedding solution for Ag NPAs with different heights. (Bottom) Bulk refractive index sensitivity for Au and Ag NPAs possessing the same shape/size characteristics.**

**Optical Dichroism**

Various methods have demonstrated the ability to align rod-like nanostructures by incorporating them into a polymer matrix to create nanocomposite films possessing polarization dependent optical properties. Dirix et. al used stretching of a polymer-NP nanocomposite film to create a "pearl-necklace" alignment of the constituent Ag NPs [18]. As a result of this induced alignment, the nanocomposite film achieved very distinct colors when viewed using linearly polarized light. Therefore, with the ability of this NIL technique to control the LSPR response of NPAs through composition and relative orientation of constituent nanostructures, tailored dichroic color filters can be designed and reliably reproduced.

To demonstrate this possibility, Figure 2.8 shows the polarization dependent response of a Au NPA fabricated using an A90B nanoblock mold characterized by a periods of 220 nm and 750 nm. The constituent Au NPs are characterized by a nominal length and width of 330nm and 60nm respectively and a height of 20 nm. For light linearly polarized along the short axis of the NPs, the resonance is found to occur at 580 nm. Conversely, light polarized along the long axis of the structure yields a resonance at the lowest energy. These two distinct plasmon modes are akin to the transverse (higher energy) and modes found in rod-like or ellipsoidal metallic nanostructures. The ability to distinguish the two modes with a collection of nanostructures possessing a diminutive

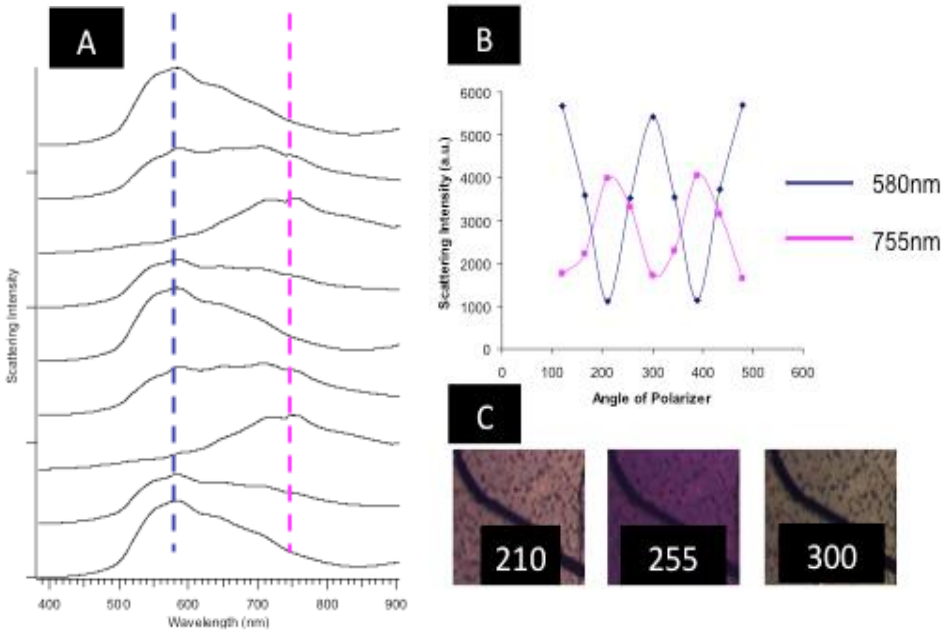


**Figure 2.8 Extinction spectra corresponding to light polarized along the short axis (transverse mode) and long axis (longitudinal mode) of the NPA. (*Inset)* Offset extinction spectrum of Au NPA**

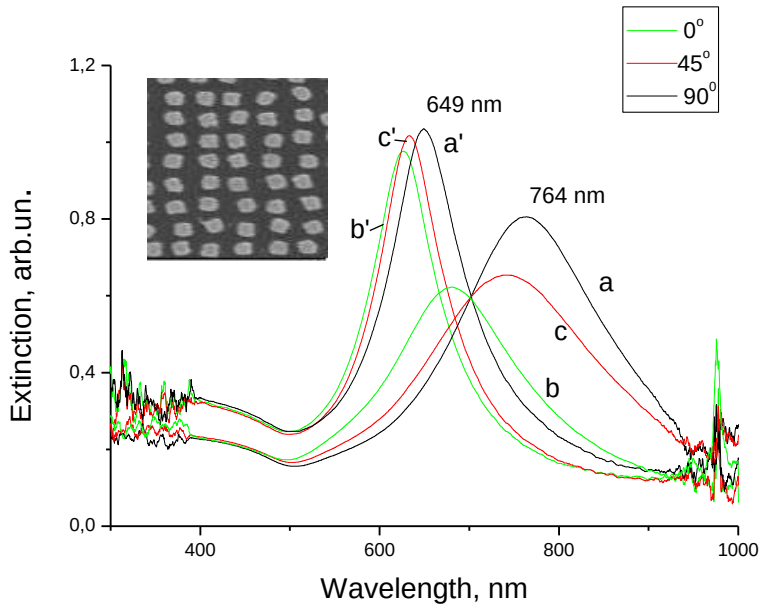


**Figure 2.9 Extinction spectra showing changes in NPA dichroism resulting from induced orientational nonuniformity. (a,b,c denotes long-axis, short-axis and cross polarization. Prime denotes spectra recorded after piranha treatment (Inset) SEM of Au NPA with a Ti adhesion layer after exposure to pirahna solution resulting in angular and lateral displacements of constituent NPs.**

shape anisotropy is a direct result of the orientational control afforded by the NIL fabrication technique as opposed to the ensemble average response of chemically synthesized nanostructures. This shape anisotropy can be attributed to slight differences in etching characteristics during mold fabrication using orthogonal imprints with a single one-dimensional grating mold.

The strong dependence of NPA dichroism on the orientation uniformity is highlighted in Figure 2.9. The strong dichroic properties of the Au NPA (height=20 nm, in-plane dimensions =115 nm x128 nm) are reduced by perturbing the orientation/position of the constituent NPs. This was accomplished by soaking the substrate in pirhana solution to dissolve the Ti underlayer used for adhesion and using surface tension forces during sample drying to produce small NP movements.

**Distance-Dependent Refractive Index Sensitivity**

The utilization of nanoblock arrays for biosensing applications relies heavily on their distant-dependent sensitivity to dielectric changes. The typical approach to using nanoparticles as transducers involves immobilizing a ligand on the surface that has a binding affinity to a target biomolecule e.g. antigen-antibody interactions. The shift of the resonance peak is directly correlated to the effective refractive index (e.g. thickness, density, component refractive indices) of the resulting biofilm. The sensing volume for plasmonic NPA is expected to be much smaller than SPR associated with planar films that typically possess evanescent field decay lengths on the order of a few hundred nanometers depending on the excitation wavelength, coupling configuration and optical properties of the film.

To mimic the presence of thin biomolecular films and ascertain the sensing volume of our NPA systems, we measured the response of the NPAs to silicon dioxide adlayers deposited using e-beam evaporation. Figure 2.10 shows the distance-dependent response for Au nanoblock arrays possessing heights of 40 nm, 60 nm and 80 nm. Similar to the findings of bulk refractive sensitivity measurements, Au nanoblock were found to be less sensitive to the corresponding dielectric changes than similar sized Ag nanoblock arrays.

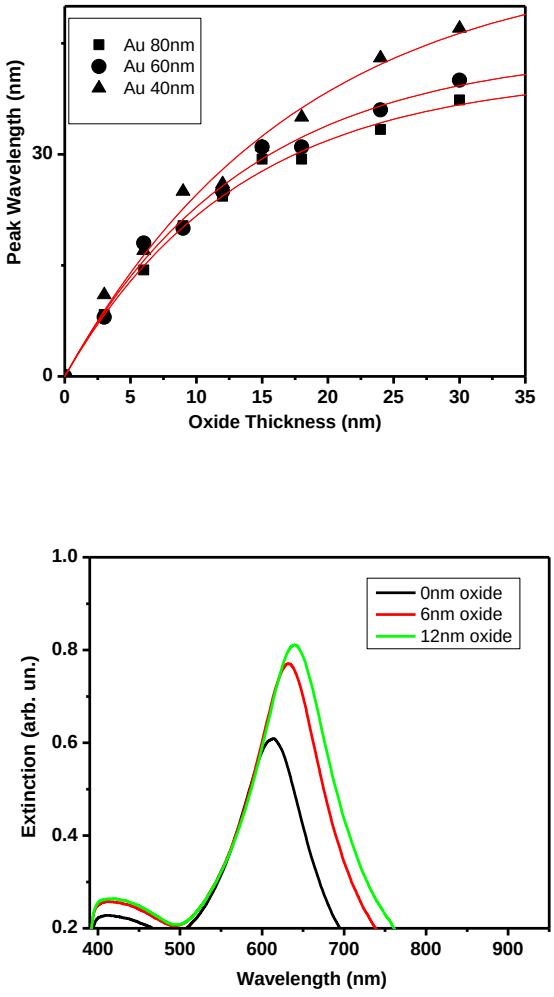


**Figure 2.10 (top) LSPR peaks for 60nm tall Au NPAs covered with different thicknesses of the $SiO_2$ Red curves represent best fit of Eq. 2.2 for $n_E$=1 and $n_A$=1.46. (bottom) LSPR peak wavelength shift $\Delta\lambda_{max}$ as a function of $SiO_2$ (n=1.46) coating thickness.**

$$\Delta\lambda_{max} = m(n_A - n_E)\left(1 - \exp\frac{-2d}{l_d}\right) \qquad (2.2)$$

| Au nanoparticle height (nm) | Refractive Index Sensitivity (nm/RIU) | Field Decay Length (nm) |
|---|---|---|
| 40nm | 123.20 | 35.26 |
| 60nm | 96.27 | 27.54 |
| 80nm | 89.03 | 26.53 |

**Table 2.2 Refractive index sensitivity (m) and field decay length ($l_d$) based on fit to equation 2.2 with $n_A$=1.46 and for $SiO_2$ and $n_E$ for air (n=1) ambient**

## Estimation of SERS Enhancement Factor

The ability of these NIL fabricated NPAs to act as SERS substrates is demonstrated in through comparison of the Raman spectra from a neat sample of 1-Phenyloctane on pyrex glass and Ag square nanostructures possessing a LSPR wavelength of 663 nm. Figure 2.11 shows an enhancement of the Raman spectrum when collected using the NPA and the raw spectrum obtained on clean pyrex glass is amplified by a factor of 3 for clarity. Consequently, a number of bands in the Raman shift region 1000-1600 $cm^{-1}$ ($\lambda$=675-704 nm) become discernible in the spectrum obtained on the NPA that were not observed in the unenhanced spectrum.

The figure of merit often used to compare SERS substrates is the enhancement factor (EF) which is defined as the ratio of the signal intensities normalized by the number of excited molecules. Based on the 1600 $cm^{-1}$ Raman band, there is

approximately an 8-fold Raman signal increase using the Ag NPA. It is important to note that the LSPR E-field enhancement for NPAs only impacts molecules within ~25 nm of the surface based on nominal E-field decay lengths. This results in a probe volume that is approximately $10^4$ smaller than the solution Raman signal and a total EF for our system of approximately $10^5$.

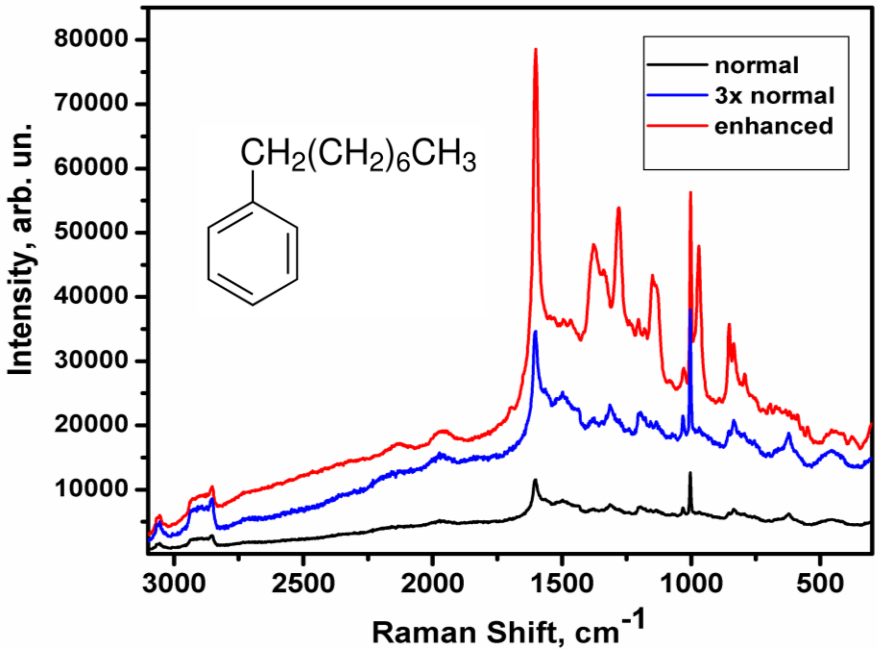


**Figure 2.11 Comparison of enhanced and unenhanced Raman spectra of neat 1-Phenyloctane demonstrating the ability of NIL-fabricated Ag NPAs to function as SERS substrates. LSPR peak wavelength for Ag NPA was 663nm yielding an EF of ~$10^4$**

Previous studies directly related to this enhancement effect have reported the enhancement factors for both changes in excitation wavelength and LSPR conditions at various locations on samples possessing different levels of homogeneity were ascertained [37, 38]. Evidence of the electromagnetic mechanism for SERS was found as the bands exhibit maximal enhancement when the LSPR peak wavelength is in between the incident and stokes-shifted radiation permitting the enhancement of both entities.

Moreover, the NSL-derived NPAs used in these studies possessed a surface coverage of approximately 7%, representing only about a quarter of the coverage realized by our NIL nanocube array (≈26% in the present case). While our current plasmonic nanostructures do not necessarily possess remarkably high local field enhancements as found at sharp tips of triangular nanostructures fabricated using NSL or small gaps found in metal aggregates ("hot spots"), however they can offer increased surface coverage that leads to a modest and reproducible 'average SERS' effect.

**Probing NPAs using Spectroscopic Ellipsometry (SE)**

The ability to improve detection sensitivity of SPR-based systems using phase-sensitive techniques has been previously demonstrated. Specifically, phase-sensitive techniques methods have been demonstrated as a useful approach based on the polarization-dependent coupling of light to SPR modes discussed earlier. This suggests that the dichroic nature of our uniformly-oriented nanoblock arrays affords an opportunity to utilize a polarization-dependent measurement technique such as ellipsometry, a phase-sensitive measurement technique that has been proven effective in analyzing the growth and morphology of thinfilms down to submonolayer coverage. While there are various ellipsometric configurations with each possessing its own limitations in terms of data, spectroscopic ellipsometry (SE) has been widely used for metrology based on the polarization dependent optical properties of structured media. Therefore, SE is a viable technique to study the relative amplitude and phase relationship of the polarization dependent LSPR.

Along with the benefit of being a nondestructive optical measurement technique, ellipsometry provides additional benefits that are relevant to the use of NPs as sensor

transduction elements. Most notable of these benefits is the ability to provide amplitude ratios and relative phases for orthogonal polarization states which minimizes the detrimental influence of light source instability which allows for improved signal-to-noise ratios for each measurement (i.e. higher detection sensitivity).

In order to explore the feasibility of using SE with our nanoblock arrays, we start by looking at Au NPAs with a rectangular shape (Figure 2.2B). Specifically, the NPs possess a height of 25 nm with in-plane dimensions of 115 nm and 128 nm. This slight anisotropy of the structure causes light polarized along the longer in-plane axis of the rectangular NPs to excite LSPs at longer resonant wavelengths than light polarized along a shorter axis as shown in Figure 2.12.

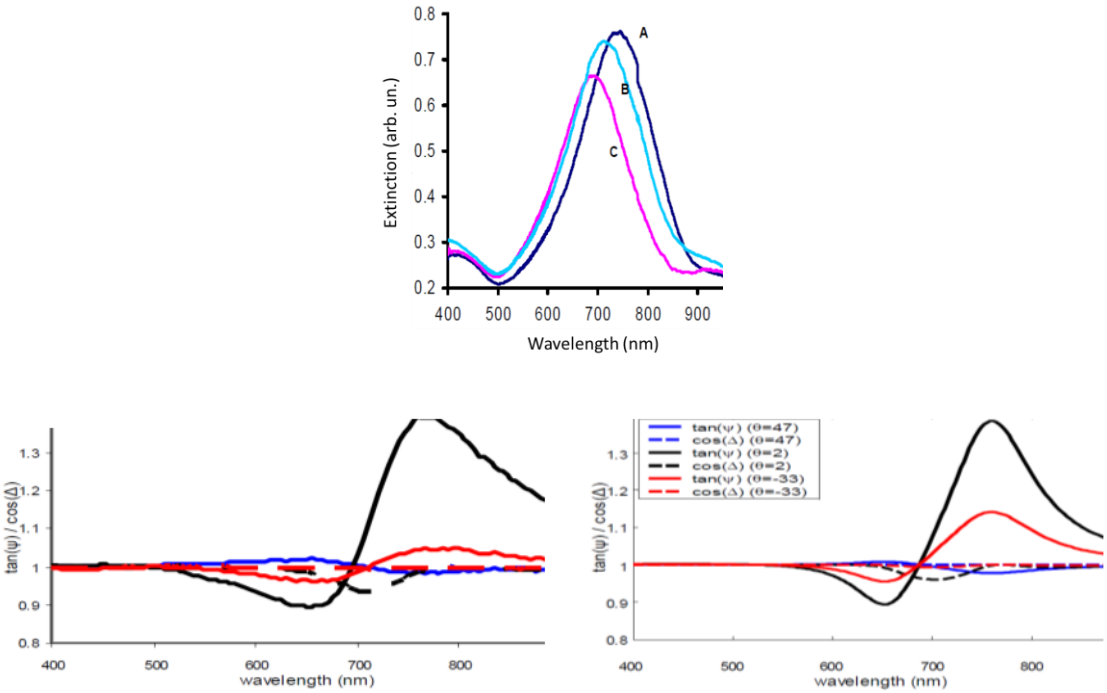


**Figure 2.12 Top: Measured extinction spectrum of the Au nanoblock array where spectrum A is measured for excitation light polar. Bottom: (left) Measured and (right) calculated results of the Au nanocube array from transmission ellipsometry with different angle of orientation of nanocubes θ where solid curves represent tan(ψ) and dashed curves represent cos(Δ).**

To acquire information for both the phase and amplitude change of light passing through the arrays of gold NPs with rectangular shape, we used SE in transmission mode at normal incidence in our experiment. SE measures the complex ratio of transmittance ρ of two orthogonally linear polarization states of light, with tan(ψ) representing the magnitude and Δ representing the phase angle of ρ. The angle of orientation (θ) of the rectangular NPs is defined as the angle between the shorter axis of rectangular NPs and the ellipsometer defined axis of p-polarization.

In order to interpret the measured SE results of the rectangular NPs, we modeled the optical transmission though the NP sample using Jones matrices as illustrated in Figure 2.13. The LSPR is assumed to give transmittance $t_L$ and $t_S$ along the long and short axis of the rectangular NPs respectively. By appropriate coordinate transformations (Figure 2.13), the overall Jones matrix and the ratio of complex orthogonal transmission can be obtained.

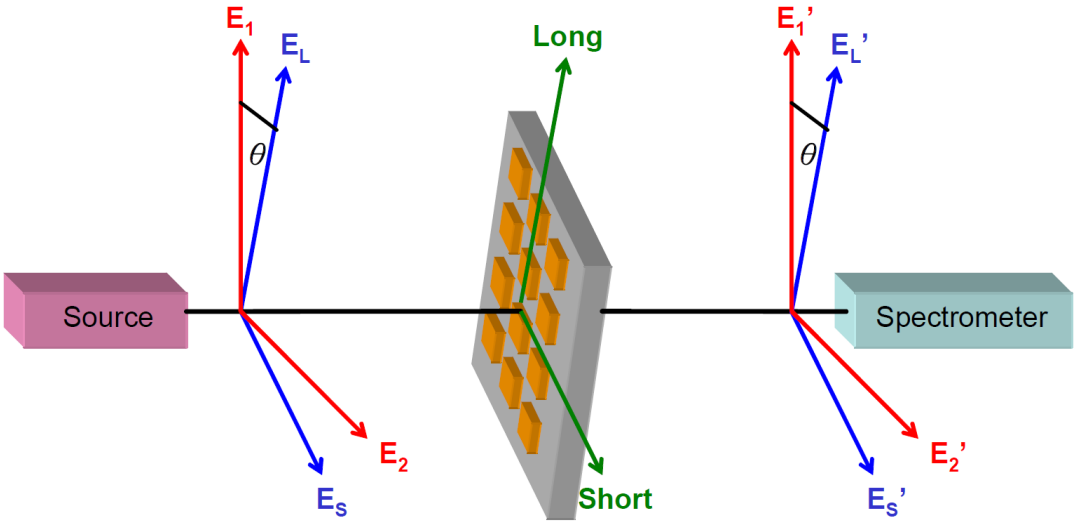


**Figure 2.13** Configuration of transmission SE and construction of Jones matrices

Writing transmission coefficient $t$ in the form of $e^{\alpha+i\delta}$ for both polarizations to account for the amplitude and phase change for light transmitted through the NP array, the real part of the exponent $\alpha_L$ and $\alpha_S$ can be extracted from the extinction spectra in Figure 2.12. However, the phase information cannot be obtained through experiment directly. To obtain the phase shift $\delta_L$ and $\delta_S$, we treat the rectangular NPs array as an effective media with susceptibility $\chi$. The imaginary part of the susceptibility ($\chi''$) can be calculated from absorption coefficient $\alpha$, and the real part ($\chi'$) can be calculated through the use of Kramers-Kronig relations. Phase shift $\delta$ can thus be retrieved from $\chi'$. With complete description of transmittance $t_L$ and $t_S$, the complex ratio of transmittance $\rho$ and therefore $\tan(\psi)$ and $\Delta$ can be calculated, as shown in Figure 2.13. Using this method, excellent agreement with the experimental results has been obtained. This model can help predict the sensitivity of ellipsometrically probed LSPR to their structural characteristics and dielectric environments with the understanding of both amplitude and phase information.

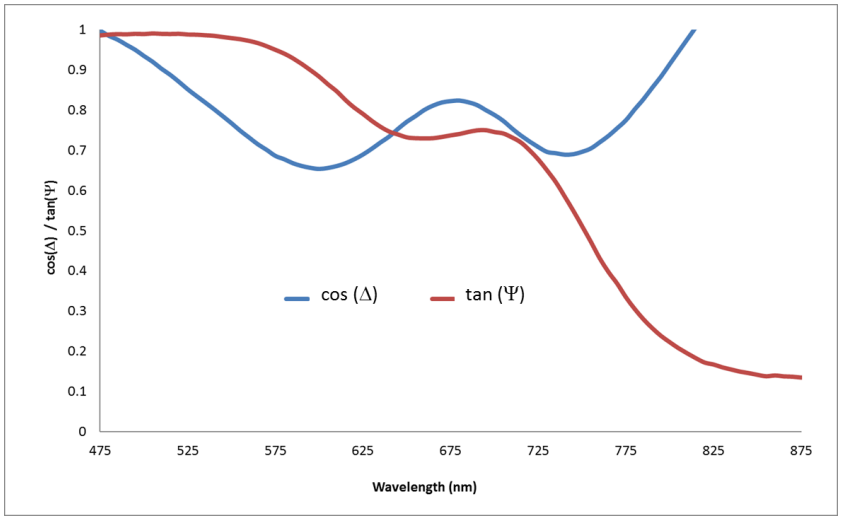


**Figure 2.14 Measured spectroscopic ellipsometry parameters for a Au NPA (height = 20 nm) created using the A45A scheme.**

The phase difference in rectangular NP array is relatively small due to the slight asymmetry of the structure. However, for the diamond NP arrays produced using an A45A scheme, the optical response is more pronounced. The measured phase angle $\Delta$, which represents the phase shift in transmission coefficients of p-polarized and s-polarized light, can exceed $\pi/4$ near plasmonic wavelengths. Compared to the thickness of an optical retarder made of crystal which is usually several microns thick, the thickness of NPs is only 20 nm. The diamond NPAs can be potentially used to fabricate compact integrated optical devices.

**Summary**

In this work, we demonstrated a very powerful and flexible approach to fabricating large-area, uniformly-oriented noble metal NPAs using NIL and one-dimensional gratings. The inherent orientational control of this fabrication technique creates NPAs that exhibit various degrees of optical dichroism depending on the aspect ratio of the constituent NPs. The dichroic properties of the NPAs were further highlighted through the use of spectroscopic ellipsometry, which affords the ability to ascertain the relative phase of orthogonal plasmonic modes. The demonstrated fabrication approach and the associated attributes of the NPAs are relevant to numerous LSPR application areas including tuneable filters, LSPR biosensors, and SERS.

## References


[1] M. D. Stewart and C. G. Willson, "Imprint materials for nanoscale devices," *Mrs Bulletin,* vol. 30, pp. 947-951, Dec 2005.

[2] H. Schift, "Nanoimprint lithography: An old story in modern times? A review," *Journal of Vacuum Science & Technology B,* vol. 26, pp. 458-480, 2008.

[3] T. Higashiki, T. Nakasugi, and I. Yoneda, "Nanoimprint Lithography for Semiconductor Devices and Future Patterning Innovation," *Alternative Lithographic Technologies Iii,* vol. 7970, 2011.

[4] L. J. Guo, "Recent progress in nanoimprint technology and its applications," *Journal of Physics D: Applied Physics,* vol. 37, pp. R123-R141, 2004.

[5] A. D. Taylor, B. D. Lucas, L. J. Guo, and L. T. Thompson, "Nanoimprinted electrodes for micro-fuel cell applications," *Journal of Power Sources,* vol. 171, pp. 218-223, 2007.

[6] B. D. Lucas, J.-S. Kim, C. Chin, and L. J. Guo, "Nanoimprint Lithography Based Approach for the Fabrication of Large-Area, Uniformly-Oriented Plasmonic Arrays," *Advanced Materials,* vol. 20, pp. 1129-1134, 2008.

[7] A. M. Lopatynskyi, V. K. Lytvyn, V. I. Nazarenko, L. J. Guo, B. D. Lucas, and V. I. Chegel, "Au nanostructure arrays for plasmonic applications: annealed island films versus nanoimprint lithography," *Nanoscale research letters,* vol. 10, pp. 1-9, 2015.

[8] V. Chegel, B. Lucas, J. Guo, A. Lopatynskyi, O. Lopatynska, and L. Poperenko, "Detection of biomolecules using optoelectronic biosensor based on localized surface plasmon resonance. Nanoimprint lithography approach," *Semiconductor Physics, Quantum Electronics & Optoelectronics,* vol. 12, pp. 91-97, 2009.

[9] R. Zia, J. A. Schuller, A. Chandran, and M. L. Brongersma, "Plasmonics: the next chip-scale technology," *Materials Today,* vol. 9, pp. 20-27, 7// 2006.

[10] J. Homola, S. S. Yee, and G. Gauglitz, "Surface plasmon resonance sensors: review," *Sensors and Actuators B-Chemical,* vol. 54, pp. 3-15, Jan 25 1999.

[11] H. A. Atwater, S. Maier, A. Polman, J. A. Dionne, and L. Sweatlock, "The new "p-n junction". Plasmonics enables photonic access to the nanoworld," *Mrs Bulletin,* vol. 30, pp. 385-389, MAY 2005.

[12] S. A. Maier, "Plasmonics - Towards subwavelength optical devices," *Current Nanoscience,* vol. 1, pp. 17-23, JAN 2005.

[13] M. D. Malinsky, K. L. Kelly, G. C. Schatz, and R. P. Van Duyne, "Nanosphere lithography: Effect of substrate on the localized surface plasmon resonance spectrum of silver nanoparticles," *Journal of Physical Chemistry B,* vol. 105, pp. 2343-2350, Mar 29 2001.

[14] J. J. Mock, M. Barbic, D. R. Smith, D. A. Schultz, and S. Schultz, "Shape effects in plasmon resonance of individual colloidal silver nanoparticles," *Journal of Chemical Physics,* vol. 116, pp. 6755-6759, APR 15 2002.

[15] J. J. Mock, D. R. Smith, and S. Schultz, "Local refractive index dependence of plasmon resonance spectra from individual nanoparticles," *Nano Letters,* vol. 3, pp. 485-491, APR 2003.

[16] K. H. Su, Q. H. Wei, X. Zhang, J. J. Mock, D. R. Smith, and S. Schultz, "Interparticle coupling effects on plasmon resonances of nanogold particles," *Nano Letters,* vol. 3, pp. 1087-1090, AUG 2003.

[17] B. K. Canfield, S. Kujala, M. Kauranen, K. Jefimovs, T. Vallius, and J. Turunen, "Remarkable polarization sensitivity of gold nanoparticle arrays," *Applied Physics Letters,* vol. 86, pp. -, MAY 2 2005.

[18] Y. Dirix, C. Bastiaansen, W. Caseri, and P. Smith, "Oriented pearl-necklace arrays of metallic nanoparticles in polymers: A new route toward polarization-dependent color filters," *Advanced Materials,* vol. 11, pp. 223-+, Feb 11 1999.

[19] C. L. Haynes and R. P. Van Duyne, "Dichroic optical properties of extended nanostructures fabricated using angle-resolved nanosphere lithography," *Nano Letters,* vol. 3, pp. 939-943, Jul 2003.

[20] A. D. McFarland and R. P. Van Duyne, "Single silver nanoparticles as real-time optical sensors with zeptomole sensitivity," *Nano Letters,* vol. 3, pp. 1057-1062, Aug 2003.

[21] N. Nath and A. Chilkoti, "A colorimetric gold nanoparticle sensor to interrogate biomolecular interactions in real time on a surface," *Analytical Chemistry,* vol. 74, pp. 504-509, Feb 1 2002.

[22] A. Bouhelier, R. Bachelot, J. S. Im, G. P. Wiederrecht, G. Lerondel, S. Kostcheev, *et al.*, "Electromagnetic interactions in plasmonic nanoparticle arrays," *Journal of Physical Chemistry B,* vol. 109, pp. 3195-3198, Mar 3 2005.

[23] S. J. Oldenburg, G. D. Hale, J. B. Jackson, and N. J. Halas, "Light scattering from dipole and quadrupole nanoshell antennas," *Applied Physics Letters,* vol. 75, pp. 1063-1065, Aug 23 1999.

[24] L. J. Sherry, S. H. Chang, G. C. Schatz, R. P. Van Duyne, B. J. Wiley, and Y. N. Xia, "Localized surface plasmon resonance spectroscopy of single silver nanocubes," *Nano Letters,* vol. 5, pp. 2034-2038, Oct 2005.

[25] S. Y. Chou and P. R. Krauss, "Imprint lithography with sub-10 nm feature size and high throughput," *Microelectronic Engineering,* vol. 35, pp. 237-240, FEB 1997.

[26] M. T. Li, L. Chen, W. Zhang, and S. Y. Chou, "Pattern transfer fidelity of nanoimprint lithography on six-inch wafers," *Nanotechnology,* vol. 14, pp. 33-36, JAN 2003.

[27] X. Y. Lei, L. Wu, P. Deshpande, Z. N. Yu, W. Wu, H. X. Ge, *et al.*, "100 nm period gratings produced by lithographically induced self-construction," *Nanotechnology,* vol. 14, pp. 786-790, JUL 2003.

[28] Z. N. Yu, L. Chen, W. Wu, H. X. Ge, and S. Y. Chou, "Fabrication of nanoscale gratings with reduced line edge roughness using nanoimprint lithography," *Journal of Vacuum Science & Technology B,* vol. 21, pp. 2089-2092, SEP-OCT 2003.

[29] Z. N. Yu and S. Y. Chou, "Triangular profile imprint molds in nanograting fabrication," *Nano Letters,* vol. 4, pp. 341-344, FEB 2004.

[30] Z. N. Yu, W. Wu, L. Chen, and S. Y. Chou, "Fabrication of large area 100 nm pitch grating by spatial frequency doubling and nanoimprint lithography for subwavelength optical applications," *Journal of Vacuum Science & Technology B,* vol. 19, pp. 2816-2819, NOV-DEC 2001.

[31] E. M. Hicks, S. L. Zou, G. C. Schatz, K. G. Spears, R. P. Van Duyne, L. Gunnarsson, *et al.*, "Controlling plasmon line shapes through diffractive coupling in linear arrays of cylindrical nanoparticles fabricated by electron beam lithography," *Nano Letters,* vol. 5, pp. 1065-1070, Jun 2005.

[32] T. W. Ebbesen, H. J. Lezec, H. F. Ghaemi, T. Thio, and P. A. Wolff, "Extraordinary optical transmission through sub-wavelength hole arrays," *Nature,* vol. 391, pp. 667-669, FEB 12 1998.

[33] L. Y. Jiao, H. J. Gao, G. M. Zhang, G. Y. Xie, X. Zhou, Y. Y. Zhang, *et al.*, "Fabrication of metallic nanostructures by negative nanoimprint lithography," *Nanotechnology,* vol. 16, pp. 2779-2784, Dec 2005.

[34] E. M. Hicks, X. Y. Zhang, S. L. Zou, O. Lyandres, K. G. Spears, G. C. Schatz, *et al.*, "Plasmonic properties of film over nanowell surfaces fabricated by nanosphere lithography," *Journal of Physical Chemistry B,* vol. 109, pp. 22351-22358, Dec 1 2005.

[35] A. J. Haes, J. Zhao, S. L. Zou, C. S. Own, L. D. Marks, G. C. Schatz, *et al.*, "Solution-phase, triangular Ag nanotriangles fabricated by nanosphere lithography," *Journal of Physical Chemistry B,* vol. 109, pp. 11158-11162, Jun 9 2005.

[36] C. L. Haynes and R. P. Van Duyne, "Nanosphere lithography: A versatile nanofabrication tool for studies of size-dependent nanoparticle optics," *Journal of Physical Chemistry B,* vol. 105, pp. 5599-5611, 2001.

[37] C. L. Haynes and R. P. Van Duyne, "Plasmon-sampled surface-enhanced Raman excitation spectroscopy," *Journal of Physical Chemistry B,* vol. 107, pp. 7426-7433, 2003.

[38] A. D. McFarland, M. A. Young, J. A. Dieringer, and R. P. Van Duyne, "Wavelength-scanned surface-enhanced Raman excitation spectroscopy," *Journal of Physical Chemistry B,* vol. 109, pp. 11279-11285, Jun 9 2005.

# Chapter 3

# Au Nanostructure Arrays for Plasmonic Applications: Annealed Island Films Versus Nanoimpring Lithography

## Introduction

Plasmonic phenomena are widely used in optical devices [1], imaging microscopy [2], biosensing [3-5], and medical diagnostics [6-8]. Improvement of sensitivity, even down to single molecule detection limits, is needed in many applications, and this problem demands a solution at the present moment. One of the possible ways to obtain general sensitivity enhancement for multiple applications is to fabricate nanopatterned plasmonic substrates capable of generating strong local electromagnetic fields, or, in other words, offering significant plasmonic enhancement (PE), due to occurrence of localized surface plasmon resonance (LSPR) phenomenon in highly conductive metal nanoparticles. It was shown both theoretically and experimentally that enhanced local field provides signal amplification for LSPR [9-11], surface-enhanced Raman scattering (SERS) [10, 12], surface-enhanced fluorescence (SEF) [13-15], and surface-enhanced infrared absorption (SEIRA) [16, 17] techniques. The peculiarity of PE accompanying LSPR is that enhanced field is concentrated in confined space with nanometer dimensions (‘hot spots’) [18] phenomenon, which depends on nanostructure size, shape, and material properties [19, 20].

Nanostructures enabling the PE effect can be fabricated using a multitude of methods [21] . A simple and commonly used approach involves highly conductive, continuous film possessing surface roughness as effective plasmonic amplifiers; however, this method does not yield the ability for spectral tuning, and, consequently, the process of enhancement cannot be applied for matching with molecular resonances that is preferable for a number of spectroscopic techniques. The benefit of spectrally controlled nanostructured PE surfaces is obvious as only uniform surface-bound nanostructure arrays (nanochips) with known surface 3D geometry can provide a real possibility to perform preliminary estimation of final PE parameters when using this technique and ensure their stability and reproducibility. In this present work, two different approaches for nanostructure fabrication were used - a method based on gold island film deposition with subsequent thermal annealing and nanoimprint lithography (NIL) technique.

The most evident advantage of the latter method is an exploitation of templates with relatively large linear dimensions and sub-10-nm resolution [22] for nanostructure preparation that makes NIL suitable for fabrication of uniformly oriented and homogeneous gold nanostructure arrays (NSA) with controlled nanoparticle size, shape, and spacing. However, due to the associated high costs for NIL technique exploitation in terms of equipment needed for NIL template fabrication and the nanoimprinting process itself, the development of an alternative technique which can be the basis for PE nanochip is of considerable interest. Here, we compare the two abovementioned methods of Au NSA fabrication from the point of view of LSPR spectral measurements and PE modeling.

## Methods

### Fabrication of Random NSA Samples

We have adapted the PE nanochip fabrication technique based on gold island film deposition with subsequent thermal annealing [23], which is an affordable NSA preparation method yielding satisfactory results. Briefly, gold island films of varying thickness (5 to 15 nm) were obtained by thermal evaporation in vacuum on precleaned microscope glass substrates ($n$ = 1.51). After island film deposition, samples were annealed at 550 °C for 6 hours in $N_2$ atmosphere. As a result of annealing, the gold film color changed from blue of different intensity to blue, violet, and pink (depending on the film thickness) that confirms the formation of separated gold nanoparticles having different sizes depending on the initial island film thickness values (see atomic force microscopy (AFM) images in Figure 3.1).

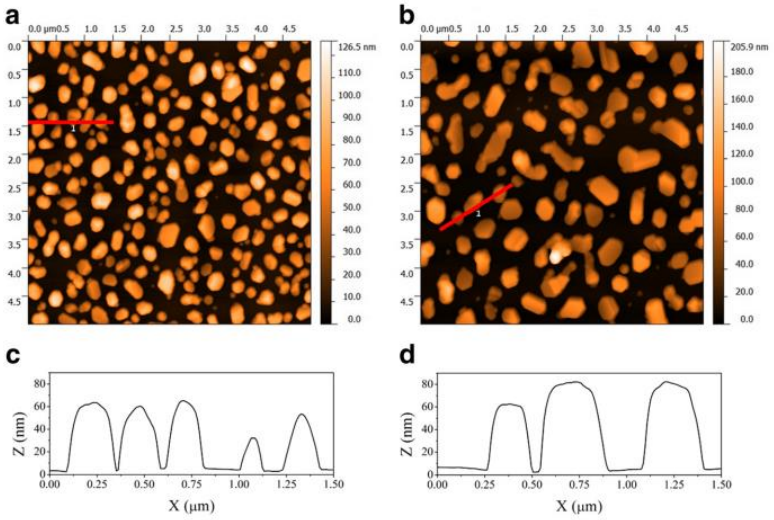


**Figure 3.1 AFM characterization results for random gold NSA samples produced via thermal annealing of gold island films. (a, b) TOp view AFM images and (c, d) corresponding AFM profiles for random gold NSA samples R6 and R7, respectively (see Table 3.1)**

**Fabrication of Ordered NSA Samples**

Ordered gold nanoparticle arrays were produced by means of NIL technique according to the protocol described earlier [24, 25]. Briefly, Pyrex glass substrates were cleaned in a 1:1 piranha solution (30% $H_2O_2$:29% $NH_4OH$), rinsed with a copious amount of DI:$H_2O$, and dried using $N_2$. The resist was spincoated to the appropriate thickness on the substrates, baked for solvent removal, and imprinted using the template. After nanoimprinting and sample separation, the residual polymer layer was removed using $O_2$ plasma reactive-ion etching. Au metallization was accomplished using an electron beam evaporator. Lift-off was performed by soaking the samples in acetone and using an ultrasonic bath. After completion of lift-off, samples were rinsed with methanol and isopropanol and dried with $N_2$. This technique can be used to create a variety of structures by simply using different one-dimensional gratings (i.e., with various duty cycles or periods) and relative angular orientation of the gratings for successive imprints to create different NIL templates [24].

Structural characteristics of ordered NSA were investigated using atomic force microscopy method. NIL fabricated NSA samples of different geometry were studied. These samples were comprised of parallelepiped-shaped nanoparticles, located in an ordered array with square or rectangular lattice. AFM images of nanostructure arrays fabricated using the mentioned technique are shown in Figure 3.2.

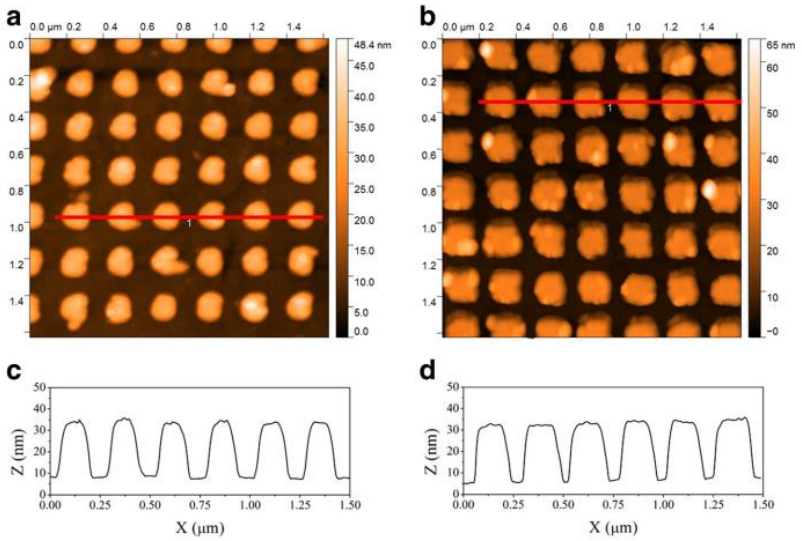


**Figure 3.2 AFM characterization results for ordered gold NSA samples produced using NIL. (a,b) Top view AFM images and (c,d) corresponding AFM profiles for ordered gold NSA samples O2 and O4, respectively (see Table 2)**

| NSA sample | Peak position in extinction spectrum (nm) | Average equivalent diameter (nm) | Average height (nm) | Average interparticle distance (nm) |
|---|---|---|---|---|
| R1 | 576 | 56 | 27 | 93 |
| R2 | 582 | 56 | 28 | 104 |
| R3 | 585 | 85 | 35 | 137 |
| R4 | 604 | 143 | 35 | 216 |
| R5 | 633 | 152 | 47 | 228 |
| R6 | 680 | 235 | 53 | 346 |
| R7 | 733 | 330 | 61 | 414 |
| R8 | 776 | 470 | 91 | 576 |
| R9 | 809 | 524 | 114 | 647 |

**Table 3.1 Spectral and structural characteristics of random NSA samples produced via thermal annealing of gold island films. Sample numbers follow the initial gold island film thickness increase.**

## AFM Measurements

Atomic force microscope 'NanoScope IIIa Dimension 3000' (Digital Instruments/Bruker, Santa Barbara, CA, USA) was used to study the NSA sample morphology. AFM data treatment in order to obtain NSA structural characteristics was performed using Gwyddion 2.37 software.

## Spectrophotometric Measurements

Light extinction measurements were carried out using a compact localized surface plasmon resonance spectrometer 'NanoPLASMON-003' (NanoPlasmon Devices, Elmhurst, IL, USA) possessing a spectral range of 400 to 1,100 nm and compatible with nanochips of various size (within the limits of a 1 × 3 inch standard plain microscopic slide) in both stationary and flow real-time operation modes. Unpolarized light from a tungsten-halogen light source was incident normally to the nanochip surface and collected using an optical fiber connected to a built-in miniature spectrometer

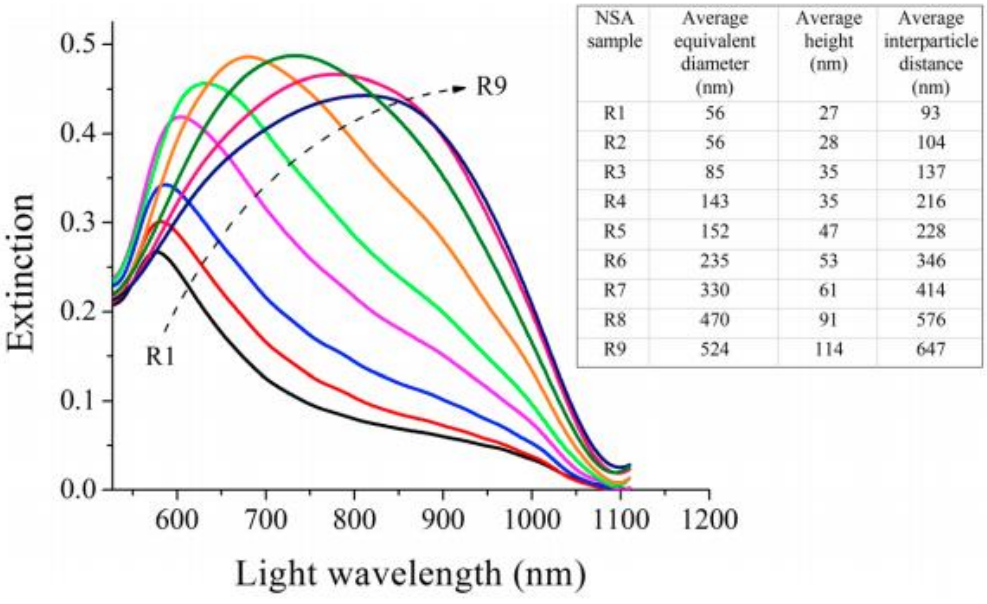


| NSA sample | Average equivalent diameter (nm) | Average height (nm) | Average interparticle distance (nm) |
|---|---|---|---|
| R1 | 56 | 27 | 93 |
| R2 | 56 | 28 | 104 |
| R3 | 85 | 35 | 137 |
| R4 | 143 | 35 | 216 |
| R5 | 152 | 47 | 228 |
| R6 | 235 | 53 | 346 |
| R7 | 330 | 61 | 414 |
| R8 | 470 | 91 | 576 |
| R9 | 524 | 114 | 647 |

**Figure 3.3 Measured extinction spectra of random NSA samples produced via thermal annealing of gold island films.**

## Theoretical Modeling of Light Extinction and Field Intensity Enhancement

To optimize the parameters required to achieve the highest PE response for the random and ordered NSAs, a theoretical study of intensity enhancement for electric component of electromagnetic field near gold nanostructure surface depending on its shape and size was carried out. According to AFM results (see Figure 3.1), nanoparticles of random NSA can be considered approximately as two-axial semi-ellipsoid in the case of smaller nanoparticles and more complex shapes in the case of larger ones. Certainly, we are aware that to fully simulate the random NSA plasmonic properties, a complete reproduction of nanostructure shape and size for each of the nanoparticle arrays is needed, which would also provide a possibility to correctly include interparticle electromagnetic interactions into the model. However, the implementation of such an approach requires costly computational resources and lengthy simulation times. To work

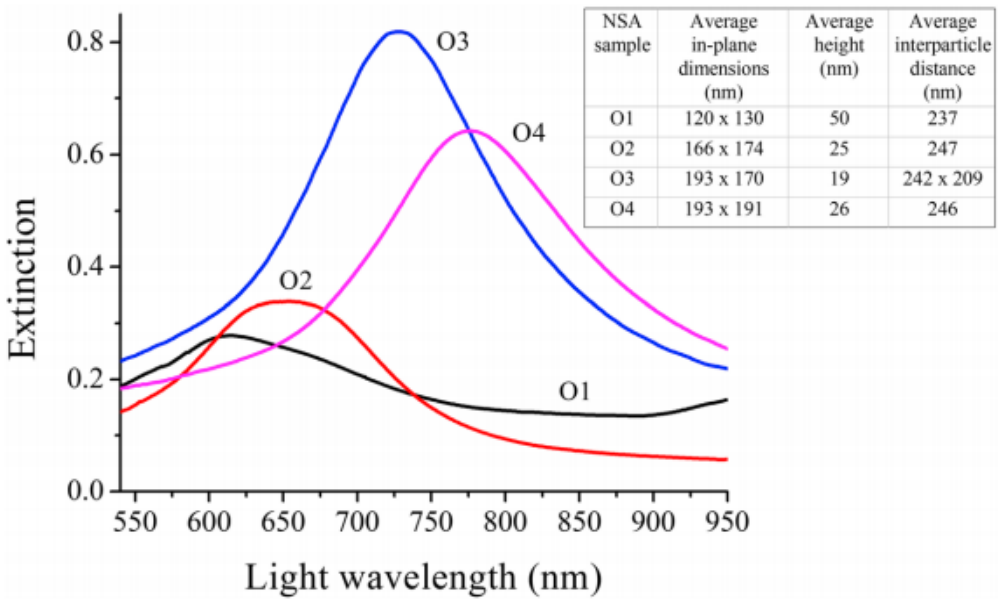


| NSA sample | Average in-plane dimensions (nm) | Average height (nm) | Average interparticle distance (nm) |
|---|---|---|---|
| O1 | 120 x 130 | 50 | 237 |
| O2 | 166 x 174 | 25 | 247 |
| O3 | 193 x 170 | 19 | 242 x 209 |
| O4 | 193 x 191 | 26 | 246 |

**Figure 3.4 Measured extinction spectra of order NSA samples produced using NIL**

around these challenges, we apply a common nanoparticle model for random NSA in the shape of two-axial semi-ellipsoid with average dimensions presented in Table 3.1.

It is well known that the greatest electric field intensity enhancements associated with highly conductive metal nanoparticles are expected in 'hot spots' on the nanoparticle surface, which are usually located on sharp corners, edges, or projections of nanoparticles [18-20]. As the semi-ellipsoid shape has no expressed regions for 'hot spots,' we anticipate the NIL method allows for the production of NSAs with the abovementioned features resulting from nanoparticles of various shapes (including parallelepiped-shaped). To compare the 'hot spots' influence on the PE level, the nanoparticles having the parallelepiped shape with a square base of the same area (i.e., having the same equivalent diameter) and same height (effective geometrical parameters (EGP)) as their semi-ellipsoid-shaped counterparts were included in the simulation. Due to the relatively sparse character of investigated NSA samples (surface-to-surface distance between nanostructures lies within the 37- to 123-nm range as determined by AFM), the nanoparticles in the array were considered to be non-interacting (the strongest coupling between nanoparticles was observed at surface-to-surface distance close to 20 nm [26]) and the individual Au nanoparticles have been selected for theoretical calculations. We are aware that the modelling of single nanostructures does not take into account the possible coupling between the adjacent nanoparticles. On the other hand, some researches require the characterization of single nanoparticles [27, 28]. However, modelling nanoparticle arrays, where cooperative plasmon modes involving multiple nanoparticles exist (e.g., dipole-dipole or higher multipole interactions), is under way, and its results will be presented in a future work.

Finally, the Au nanoparticles of semi-ellipsoid and parallelepiped shape located on glass substrates in air environment have been considered as our model system. Due to the lack of a general analytical model that fully describes the electromagnetic response of arbitrary-shaped nanoparticle, numeric methods should be used. Thus, to estimate the scattering and extinction of electromagnetic field by non-spherical Au nanoparticles, finite-difference time-domain (FDTD) method implemented in Lumerical's FDTD Solutions software was exploited. This allowed spectral distributions of local electromagnetic field intensity in the near-field of the nanoparticle and light extinction spectrum that represent the excitation of LSPR in the nanoparticle to be obtained. The full 3D FDTD model was computed for linearly polarized incident light and wavelength ranging from 400 to 2,000 nm with simulation mesh fixed at 2 × 2 × 2 nm. Linearly polarized light source was used, which is common for the case of symmetric nanoparticle shapes considered; therefore, results obtained can also be applied to unpolarized NSA illumination.

## Results

### Characteristics of Random NSA Samples

As a result of spectrophotometric measurements, light extinction spectra of the samples in air atmosphere were obtained (Figure 3.3). It was found that the peak position in the unpolarized light extinction spectrum, which corresponds to the occurrence of LSPR, shifts towards longer wavelengths with an increase in the initial gold island film thickness (see Figure 3.3 and Table 3.1). Additionally, the direct relation between lateral dimensions and height of nanostructures produced after annealing and the initial gold island film thickness was revealed. Thus, it is possible to tune the LSPR spectral position in the wavelength range from 576 to 809 nm (see Figure 3.3), and the associated PE

spectral profile, by changing the initial gold island film thickness. Obviously, considered PE nanochips fabrication technology based on gold island films with subsequent thermal annealing can be exploited while taking into account inherent technological limitations that hinder the preparation of geometrically ordered nanoparticle arrays.

| NSA sample | Peak position in extinction spectrum (nm) | Average in-plane dimensions (nm) | Average height (nm) | Average interparticle distance (nm) |
|---|---|---|---|---|
| O1 | 606 | 120x130 | 50 | 237 |
| O2 | 652 | 166x174 | 25 | 247 |
| O3 | 731 | 193x170 | 19 | 242x209 |
| O4 | 783 | 193x191 | 26 | 246 |

**Table 3.2 Spectral and structural characteristics of ordered NSA samples produced using NIL**

## Characteristics of Ordered NSA Samples

Spectral characteristics and structural parameters of ordered NSAs were obtained using the previous experimental conditions and yielded the following results (Figure 3.4, Table 3.2). Unpolarized light extinction spectra for each of the samples exhibited bands having an expressed peak with different spectral positions (from 606 to 783 nm) and extinction intensities, which mainly depend on the geometrical parameters of the nanostructures. Significant spectral shift of the LSPR band also implies the possibility of wide-range wavelength tuning using NSA fabricated by the NIL technique. Strong variation of extinction intensity should be noted as a disadvantage of such spectral tuning for both methods of NSA fabrication.

**Modeling Results**

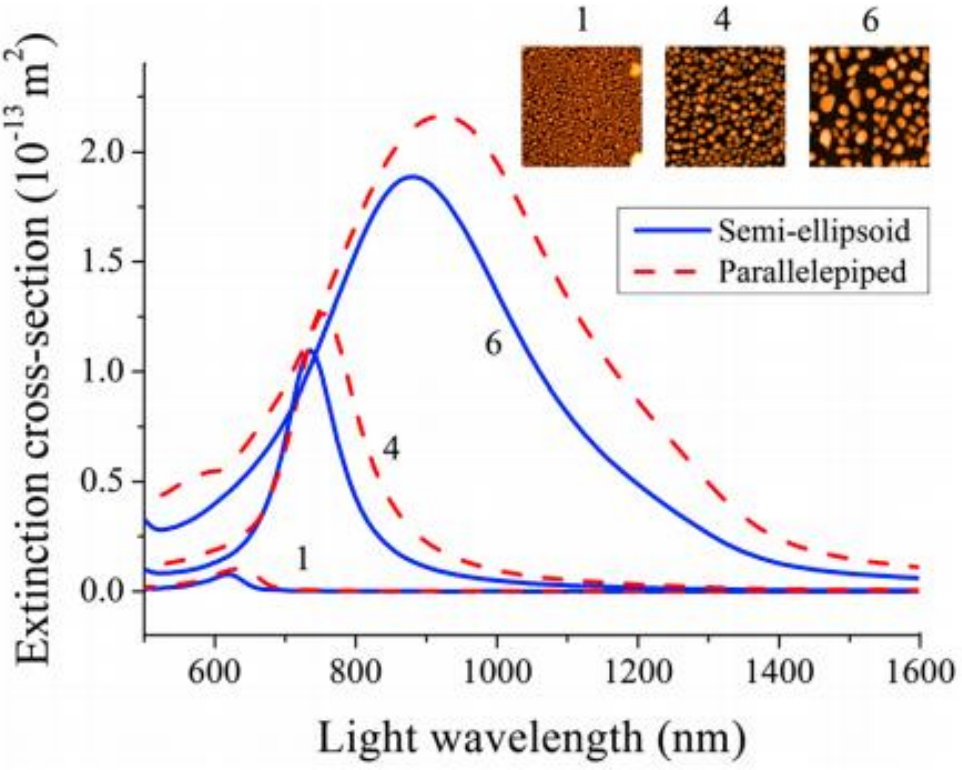


**Figure 3.5 Simulated light extinction cross-section spectra for semi-ellipsoid and parallelepiped-shaped Au nanoparticles on glass substrates.**

First, light extinction properties of model nanoparticle systems have been simulated for the two considered shapes (i.e., semi-ellipsoid and parallelepiped). Figure 3.5 shows typical light extinction spectra for both shapes with EGP corresponding to samples R1, R4, and R6 presented in Table 3.1. It is evident that simulated extinction spectra follow the same trend of red-shifting and widening upon the increase in nanoparticle dimensions as experimental extinction spectra, which can be related to the mutual influence of light scattering and secondary radiation of electrons (radiation

damping effect) [29, 30].

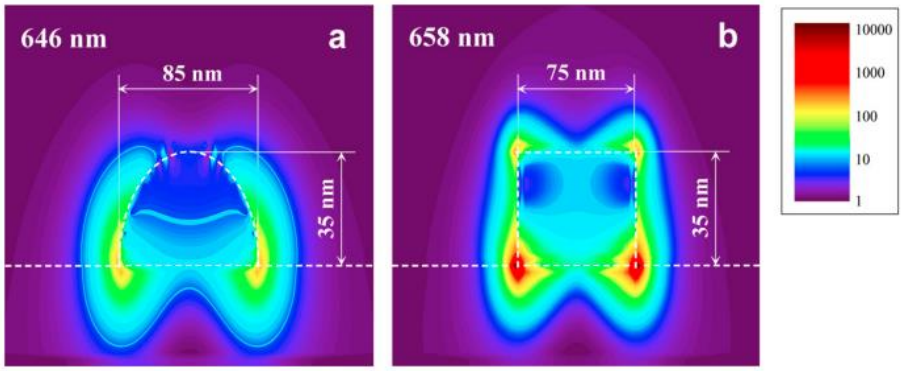


**Figure 3.6 Simulated profiles of eletric field intensity enhancement for differently shaped Au nanoparticles**

Additionally, extinction response of semi-ellipsoid and parallelepiped-shaped nanoparticles does not exhibit noticeable differences except for a permanent red-shift and marginally increased FWHM of parallelepiped-shaped nanoparticle spectrum (see Figure 3.5), which can be attributed to the shape effect. Observed difference between the experimental and modelled extinction spectra, which is most evident for random NSA, can be explained by the growing mismatch between the model semi-ellipsoid and

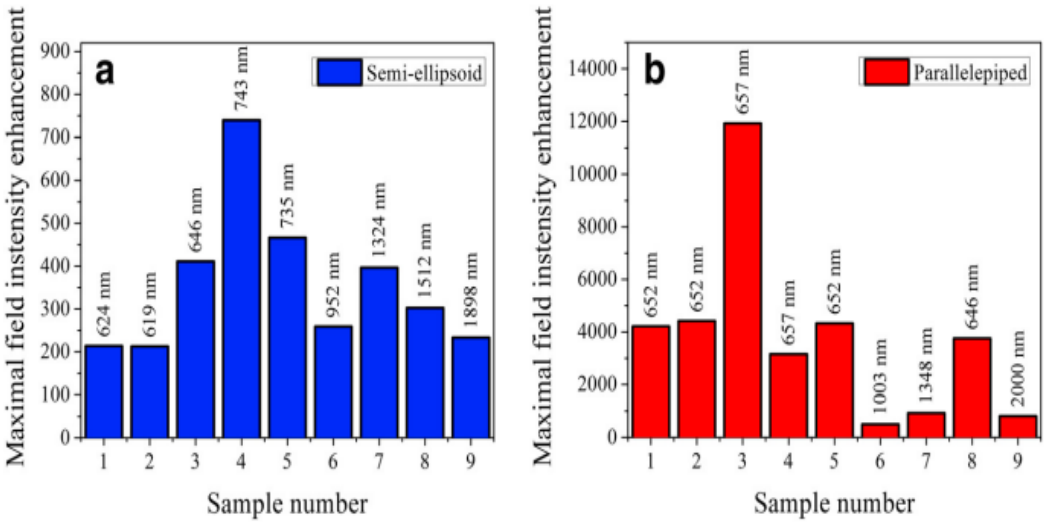


**Figure 3.7 Calculated values of maximal electric field intensity enhancement for differently shaped Au nanoparticles**

experimental nanostructure shapes with increasing nanostructures size. Additionally, the near-field interaction between nanostructures and their size distribution also contribute to the observed discrepancy between the experimental and calculated data. Nevertheless, the above mentioned trend of spectra redshifting and widening is obvious. Comparison of maximal local electric field distribution around the nanoparticles of different shapes shows that parallelepiped-shaped nanoparticles on glass substrates provide electric field intensity enhancements more than an order of magnitude greater than their semi-ellipsoidal counterparts (Figure 3.6). For example, parallelepiped nanoparticles with equivalent diameters of 85 nm and height of 35 nm exhibit maximal incident field intensity enhancement up to approximately $1.2 \times 10^4$ . In comparison, semi-ellipsoidal nanoparticles with the same EGP provide maximal electric field intensity enhancement of only about $4.1 \times 10^2$ .

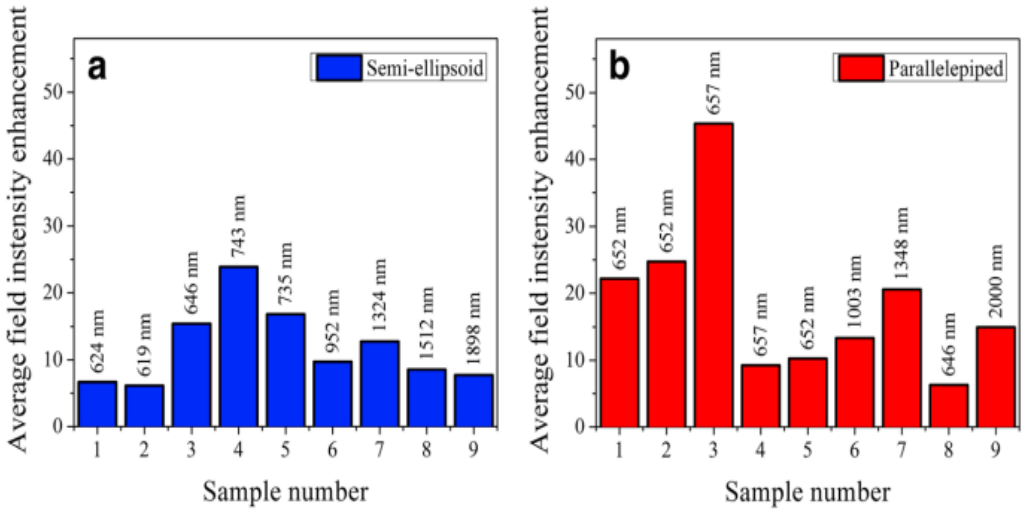


**Figure 3.8 Calculated values of average field intensity enhancement within a 25-nm vicinity of differently shaped Au nanoparticles.**

The whole set of maximal electric field enhancement values obtained for each of the nanoparticle geometries is presented in Figure 3.7. It is evident that the largest enhancement values are exhibited when equivalent diameters of both types of

nanoparticles range from 85 to 143 nm and the height of nanoparticles is 35 nm. These optimized geometrical parameters can be used for manufacturing purposes to fabricate Au NSA providing plasmonic enhancement for different applications. For a defined nanoparticle shape and geometrical parameters, maximal electric field intensity enhancement is obtained at a specific light wavelength, which was found to range fromabout 620 nm (for small nanoparticles) to near infrared region (for large nanoparticles).

Detailed light wavelength values are contained in labels in Figures 3.6, 3.7, and 3.8. It is particularly important to discuss the difference between electric field intensity enhancements for semiellipsoidal and parallelepiped nanoparticles considering not only the 'hot spots' regions but the vicinity of the entire nanoparticle surface where other objects of interest, e.g., molecular or biomolecular species, can reside. To accomplish this task, we calculated the average electric field intensity enhancements within a 25-nm vicinity (maximal value for a biomolecular monolayer) of both semiellipsoidal and parallelepiped Au nanoparticles (Figure 3.8). Interestingly, in this case, both nanoparticle shapes have demonstrated comparable average electric field enhancement values that peaked at about 24 and 45 for semiellipsoidal and parallelepiped nanoparticles, respectively. This result implies that not only NIL-fabricated nanochips but also NSA samples obtained using island film thermal annealing method can be promising as a possible PE basis for various surface-enhanced spectroscopies. The NIL NSA can be more effective for detection of small size molecules, which are able to reach 'hot spots' in the vicinity of nanostructure base.

## Conclusions

Samples of random and ordered gold nanoparticle arrays with different morphologies, which were fabricated using thermal annealing of vacuum-evaporated island films and nanoimprint lithography methods, exhibit differences in the maximal level of plasmonic enhancement. However, both nanoparticle shapes have shown comparable average enhancement values in their near vicinity. Among the considered configurations, optimal enhancement is achieved when Au nanoparticles have equivalent diameters ranging from 85 to 143 nm and height equal to 35 nm. Both techniques allow the wavelength tuning of LSPR for considered NSA samples in the range of about 200 nm.

Thermally annealed island films revealed smooth nanostructure shapes resembling semi-ellipsoids, with easy access to their surfaces by detected molecules possessing a wide range of sizes. In contrast, nanoimprint lithography produced nanostructures with sharp corners that can, on the one hand, generate ‘hot spots’ with strong PE, and, on the other hand, hinder the access of larger analyte molecules to these regions thereby creating more favorable conditions for small molecule detection. In summary, both studied fabrication approaches can find different implementations to prepare the nanostructured plasmonic arrays for a wide range of applications, such as biosensing and resonant methods using electromagnetic fields of nanostructures.

## References


[1] A. V. Kildishev, A. Boltasseva, and V. M. Shalaev, "Planar photonics with metasurfaces," *Science,* vol. 339, 2013.

[2] B. Gjonaj, J. Aulbach, P. M. Johnson, A. P. Mosk, L. Kuipers, and A. Lagendijk, "Focusing and scanning microscopy with propagating surface plasmons," *Phys Rev Lett,* vol. 110, 2013.

[3] J. N. Anker, W. P. Hall, M. P. Lambert, P. T. Velasco, M. Mrksich, and W. L. Klein, "Detection and identification of bioanalytes with high resolution LSPR spectroscopy and MALDI mass spectrometry," *J Phys Chem C,* vol. 113, 2009.

[4] M. Bauch, K. Toma, M. Toma, Q. Zhang, and J. Dostalek, "Plasmon-enhanced fluorescence biosensors: a review," *Plasmonics,* vol. 9, 2014.

[5] J. A. Ruemmele, W. P. Hall, L. K. Ruvuna, and R. P. Duyne, "A localized surface plasmon resonance imaging instrument for multiplexed biosensing," *Anal Chem,* vol. 85, 2013.

[6] A. J. Haes, W. P. Hall, L. Chang, W. L. Klein, and R. P. Duyne, "A localized surface plasmon resonance biosensor: first steps toward an assay for Alzheimer's disease," *Nano Lett,* vol. 4, 2004.

[7] B. Sciacca, A. François, M. Klingler-Hoffmann, J. Brazzatti, M. Penno, and P. Hoffmann, "Radiative-surface plasmon resonance for the detection of apolipoprotein E in medical diagnostics applications," *Nanomedicine,* vol. 9, 2013.

[8] T. Vo-Dinh, A. M. Fales, G. D. Griffin, C. G. Khoury, Y. Liu, and H. Ngo, "Plasmonic nanoprobes: from chemical sensing to medical diagnostics and therapy," *Nanoscale,* vol. 5, 2013.

[9] V. R. Dantham, S. Holler, C. Barbre, D. Keng, V. Kolchenko, and S. Arnold, "Label-free detection of single protein using a nanoplasmonic-photonic hybrid microcavity," *Nano Lett,* vol. 13, 2013.

[10] A. J. Haes, S. Zou, G. C. Schatz, and R. P. Duyne, "A nanoscale optical biosensor: the long range distance dependence of the localized surface plasmon resonance of noble metal nanoparticles," *J Phys Chem B,* vol. 108, 2004.

[11] A. I. Henry, J. M. Bingham, E. Ringe, L. D. Marks, G. C. Schatz, and R. P. Duyne, "Correlated structure and optical property studies of plasmonic nanoparticles," *J Phys Chem C,* vol. 115, 2011.

[12] D. A. Genov, A. K. Sarychev, V. M. Shalaev, and A. Wei, "Resonant field enhancements from metal nanoparticle arrays," *Nano Lett,* vol. 4, 2004.

[13] W. Deng, F. Xie, H. T. M. C. M. Baltarac, and E. M. Goldys, "Metal-enhanced fluorescence in the life sciences: here, now and beyond," *Phys Chem Chem Phys,* vol. 15, 2013.

[14] S. Xu, Y. Cao, J. Zhou, X. Wang, X. Wang, and W. Xu, "Plasmonic enhancement of fluorescence on silver nanoparticle films," *Nanotechnology,* vol. 22, 2011.

[15] Z. Zhang, P. Yang, H. Xu, and H. Zheng, "Surface enhanced fluorescence and Raman scattering by gold nanoparticle dimers and trimers," *J Appl Phys,* vol. 113, 2013.

[16] L. V. Brown, K. Zhao, N. King, H. Sobhani, P. Nordlander, and N. J. Halas, "Surface-enhanced infrared absorption using individual cross antennas tailored to chemical moieties," *J Am Chem Soc,* vol. 135, 2013.

[17] G. I. Dovbeshko, V. I. Chegel, N. Y. Gridina, O. P. Repnytska, Y. M. Shirshov, and V. P. Tryndiak, "Surface enhanced IR absorption of nucleic acids from tumor cells: FTIR reflectance study," *Biopolymers,* vol. 67, 2002.

[18] J. A. Sánchez-Gil, J. V. García-Ramos, and E. R. Méndez, "Near-field electromagnetic wave scattering from random self-affine fractal metal surfaces: Spectral dependence of local field enhancements and their statistics in connection with surface-enhanced Raman scattering," *Phys Rev B,* vol. 62, 2000.

[19] E. Hao and G. C. Schatz, "Electromagnetic fields around silver nanoparticles and dimers," *J Chem Phys,* vol. 120, 2004.

[20] J. C. Weeber, C. Girard, J. R. Krenn, A. Dereux, and J. P. Goudonnet, "Near-field optical properties of localized plasmons around lithographically designed nanostructures," *J Appl Phys,* vol. 86, 1999.

[21] "Chegel VI. Nanostructured materials for biosensor applications: comparative review of preparation methods. In: Ariga K, editor. O'Brien P, Kroto H, Nuzzo R, series editors. Manipulation of nanoscale materials: an introduction to nanoarchitectonics. RSC Nanoscience & Nanotechnology, vol. 24. Cambridge: The Royal Society of Chemistry; 2012. p. 318-55," ed.

[22] S. Y. Chou and P. R. Krauss, "Imprint lithography with sub-10 nm feature size and high throughput," *Microelectron Eng,* vol. 35, 1997.

[23] O. Kedem, A. B. Tesler, A. Vaskevich, and I. Rubinstein, "Sensitivity and optimization of localized surface plasmon resonance transducers," *ACS Nano,* vol. 5, 2011.

[24] B. D. Lucas, J. S. Kim, C. Chin, and L. J. Guo, "Nanoimprint lithography based approach for the fabrication of large-area, uniformly-oriented plasmonic arrays," *Adv Mater*, vol. 20, 2008.

[25] V. Chegel, B. Lucas, J. Guo, A. Lopatynskyi, O. Lopatynska, and L. Poperenko, "Detection of biomolecules using optoelectronic biosensor based on localized surface plasmon resonance. Nanoimprint lithography approach," *Semicond Phys Quantum Electron Optoelectron*, vol. 12, 2009.

[26] M. K. Kinnan and G. Chumanov, "Plasmon coupling in two-dimensional arrays of silver nanoparticles: II. Effect of the particle size and interparticle distance," *J Phys Chem C*, vol. 114, 2010.

[27] Y. Chen, K. Munechika, and D. S. Ginger, "Dependence of fluorescence intensity on the spectral overlap between fluorophores and plasmon resonant single silver nanoparticles," *Nano Lett*, vol. 7, 2007.

[28] M. Rycenga, X. Xia, C. H. Moran, F. Zhou, D. Qin, and Z. Y. Li, "Generation of hot spots with silver nanocubes for single-molecule detection by surface-enhanced Raman scattering," *Angew Chem Int Ed Engl*, vol. 50, 2011.

[29] M. Hu, C. Novo, A. Funston, H. Wang, H. Staleva, and S. Zou, "Dark-field microscopy studies of single metal nanoparticles: understanding the factors that influence the linewidth of the localized surface plasmon resonance," *J Mater Chem*, vol. 18, 2008.

[30] C. Noguez, "Optical properties of isolated and supported metal nanoparticles," *Opt Mater*, vol. 27, 2005.

# Chapter 4

## Detection of Biomolecules Using Optoelectronic Biosensor Based on Localized Surface Plasmon Resonance

### Introduction

Localized surface plasmon resonance (LSPR) phenomenon, as collective oscillation of free electrons in nanosized structures of high-conductive metals [1, 2], became widely attractive for the researchers since different methods of nanostructures fabrication had been developed, which give the opportunity to fabricate large nanoparticles arrays (NPAs) and nanostructured films [3, 4].

Numerous important applications of localized surface plasmon resonance phenomenon were demonstrated in recent years. Kreibig in 1995 [1] showed that the absorbance of an immobilized monolayer of gold colloids is sensitive to the refractive index of the surrounding solvent. Several experimental works related to influence of nanoparticle (NP) systems parameters (e.g. shape, size and spacing) on their extinction properties and observed optical dichroism were published recently [5-11].
Some basic methods of nanostructured film fabrication were demonstrated.

Two of the most appropriate methods, NP deposition from the colloid solution and nanosphere lithography, were rather widely used for the investigation of fundamental properties of these systems [9, 12-14]. Van Duyne *et al.* [15], Natan *et al.* [16, 17] have shown that silver or gold nanoconstructs can be created using nanosphere

lithography (NSL) on mica or glass surfaces to yield an optically detectable monolayer for the transduction of biomolecular binding events. G. Chumanov *et al.* [18] have shown the possibility of creating stable monolayers of silver nanoparticles, obtained from colloid solutions, using polymer layer that fixes low part of the nanoparticles and does not prevent the LSPR appearance on the surface of NP that is free of the polymer. Silver nanostructure arrays fabricated in such a way demonstrate extra narrow peaks in absorption spectra, which can be used to create high-sensitive biosensors. The major disadvantage of the mentioned technologies is their limitations associated with NP shape, monodispersity and reproducibility which adversely impact their viability for wide application.

In this work, we use a recently developed nanoimprint lithography technology to create uniformly oriented and homogenous noble metal NPAs with well controlled size, shape and spacing as a basis for the development of sensors for biomolecular detection. The most notable advantage of this method is the use of molds for the production of NP structures which makes nanoimprint lithography (NIL) a high-throughput and low-cost process capable for patterning large areas with sub-10 nm resolution capability [19, 20]. This method provides a general platform for rapid prototyping of different types of NPAs (shapes, size, composition and spacing) and provides simultaneous fabrication over a billion monodisperse nanoparticles in a reproductive processing sequence directly on a variety of substrates.

The use of a one-dimensional grating mold to produce two-dimensional patterns permits to obtain three-dimensional nanostructures with a defined shape that form NPA with desired optical properties. Among the wide-ranging applications of NPAs, biosensor

application appears to be one of the most promising because of the possibility to detect interaction between biomolecules in the real-time mode [21, 22]. To produce sensor structure for the detection of biomolecules, we have used NIL method for producing Au nanostructure arrays with parallelepiped shape, obtained from one-dimensional gratings. As a result, nanostructure arrays with well-defined sizes (120×130×50 nm), shape and spacing (230 nm) were obtained.

Using this approach, we demonstrate proof-of-principle of an optoelectronic biosensor to quantify biomolecular interactions in real time using a UV-visible spectrophotometer. This LSPR-sensor has minimal technological requirements, namely, the availability of an UV-visible spectrophotometer and peristaltic pump. The sensor ability of biomolecular recognition relies on the change in the extinction spectrum of NPA as a function of biomolecular adsorption to the gold surface.

Although nascent NIL-produced nanoparticle arrays result in a nonselective sensor platform, a high degree of analyte selectivity can be conferred using the specificity of surface-attached ligands and passivation of the sensor surface to nonspecific binding [23, 24]. We believe this approach can be used to extend the fundamental research on LSPR and is applicable for commercialization of technology for producing LSPR biochips.

**Theoretical Background**

Noble metal nanoparticles possess the ability to support a localized surface plasmon resonance. The electric field distribution of the excited localized surface plasmon modes and their frequencies strongly depend on the size, shape and optical constants of the particle and the dielectric properties of the surrounding medium. In the

simplest case of a spherical particle that is much smaller than the light wavelength, the polarizability of the particle is [1, 2]

$$\alpha = 4\pi\varepsilon_o R^3 \frac{\varepsilon - \varepsilon_m}{\varepsilon + 2\varepsilon_m} \tag{4.1}$$

where $\varepsilon_0$ is the dielectric permittivity of vacuum, R is the nanoparticle radius, $\varepsilon$ is the dielectric function of the particle material and $\varepsilon_m$ is the dielectric function of the medium surrounding the particle. The excitation of the dipolar localized surface plasmon mode takes place, when the frequency of the incident light equals to the frequency that corresponds to the minimum of the denominator $\varepsilon + 2\varepsilon_m$ absolute value, which results in a maximum of the polarizability spectrum.

The occurrence of LSPR leads to an increase in the extinction of light by the nanoparticles. The simplest theoretical method for modeling the optical properties – particularly, the extinction of nanoparticles – is the Mie theory for spherical particles. The extinction cross-section spectrum of the metallic sphere, the size of which is much smaller than the light wavelength, in the dipole approximation is described by the simplified Mie formula [1]:

$$\sigma_{ext}(\omega) = 9\frac{\omega}{c}\varepsilon_m^{3/2} V_p \frac{\varepsilon_2(\omega)}{[\varepsilon_1(\omega) + 2\varepsilon_m]^2 + \varepsilon_2(\omega)^2} \tag{4.2}$$

where $\omega$ is the light angular frequency, c is the light velocity in vacuum, $V_p = \frac{4}{3}\pi R^3$

is the nanoparticle volume, $\varepsilon(\omega)_1$ and $\varepsilon(\omega)_2$ are the real and imaginary parts of the particle material dielectric function. In the case of larger spherical nanoparticles, localized surface plasmon modes of higher multipole orders should be taken into account. In the framework of the Mie theory, the extinction cross-section of the spherical particle, accounting the multipole modes up to the order of L, is calculated using the following equation [1]:

$$\sigma_{ext} = \frac{2\pi}{\left|\vec{k}\right|^2}\sum_{l=1}^{L}(2l+1)\mathrm{Re}(a_l + b_l)$$

$$a_l = \frac{m\Psi_l(mx)\Psi'_l(x) - \Psi'_l(mx)\Psi_l(x)}{m\Psi_l(mx)\eta'_l(x) - \Psi'_l(mx)\eta_l(x)} \qquad (4.3)$$

$$b_l = \frac{\Psi_l(mx)\Psi'_l(x) - m\Psi'_l(mx)\Psi_l(x)}{\Psi_l(mx)\eta'_l(x) - m\Psi'_l(mx)\eta_l(x)}$$

where $\vec{k}$ is the wavevector of light in surrounding medium, $m = n / n_m$ , $n$ is the complex refractive index of particle material, nm is the real refractive index of surrounding medium, is $x = \left|\vec{k}\right|R$ the size parameter and $\Psi_l(z)$ and $\eta_l(z)$ are Riccati-Bessel functions. The prime indicates differentiation with respect to the argument of the function.

To estimate the LSPR properties of nanoparticles in the shape of parallelepiped, one should consider the contribution of all localized surface plasmon modes that are excited by the incident light. The resulting polarizability is calculated as the sum over these modes labeled by *i* [1]:

$$\alpha = \varepsilon_o V \sum_{i=1}^{N_i} \frac{C_i(\varepsilon - \varepsilon_m)}{\varepsilon_m + L_i(\varepsilon - \varepsilon_m)} \qquad (4.4)$$

where $V$ is the volume of the particle, $C_i$ are the oscillator strengths and $L_i$ are the geometrical depolarization factors.

To simplify this approach, the use of analytical methods for calculation of nanoparticle extinction properties is preferable. Two promising methods are the Green function formalism in its analytical approach [25] or the quasi-crystalline approximation (QCA) of the theory of multiple scattering of waves [26], which allows accounting the interparticle interaction. However, both aforementioned methods have some disadvantages, because the former does not take into account the interaction between nanoparticles, whereas the second one can characterize only spherical (ellipsoidal) objects. The known discrete dipole approximation (DDA) method [27] does not have these disadvantages; however, due to requirement of supercomputer resources we do not consider it.

## Mold and Sample Fabrication

### Mold Fabrication

A thin 10 nm film of Cr serving as the reactive ion etching (RIE) mask layer was electron beam evaporated on 200 nm thermally grown $SiO_2$. The nanoimprint resist (MicroResist MR-I 8020) was spincoated onto the substrate to the appropriate thickness (determined by mold depth, duty cycle and period), baked on hotplate (140 °C; 5 min) to remove residual solvent and imprinted in a custom-built nanoimprinter (4.6 MPa; 5 min; 180 °C). After separation of the mold and substrate, the residual polymer was removed in

$O_2$ plasma and the pattern was transferred to the Cr layer using RIE ($Cl_2/O_2$; 200 W). The resist was stripped using acetone incubation, rinsed with methanol and isopropanol and dried using a stream of $N_2$ gas.

The above process steps were repeated for the second imprint and the 200 nm SiO2 was subsequently reactive-ion etched ($CHF_3$; 150 W) using the patterned Cr mask. After etching, the Cr mask was removed using a wet chromium etchant (CR-14; Cyantek Co.), rinsed with a copious amount of deionized water (DI:$H_2O$) and dried with $N_2$. The mold was then prepared for imprinting by vapor-phase surfactant treatment to reduce mold-polymer adhesion.

The process illustrated in Figure 4.1 describes the general approach for creation of large-area molds that are used to fabricate NPAs afterwards. Nanostructured molds are utilized through usual NIL processing steps that include imprinting, residual polymer removal, metallization and lift-off. This technique can be used to create a variety of structures by simply using different one-dimensional gratings (i.e. with various duty cycles or periods) and relative angular orientation of the gratings for successive imprints. The examples of the application of described method are shown in Figure 4.3, where the same grating mold is used to create a lattice of square and diamond-shaped pillars (Figures 4.3 a, b), while structures presented in Figures 4.3 c, d are produced by application of different grating molds.

**Sample Fabrication**

Pyrex glass substrates with the thickness 0.5 mm ($n$ = 1.474) were cleaned in a 1:1 piranha solution (30 % $H_2O_2$:29 % $NH_4OH$), rinsed with a copious amount of DI:$H_2O$

and dried using $N_2$. The resist was spincoated to the appropriate thickness on the substrate, baked on a hotplate for solvent removal and imprinted.

After nanoimprinting and sample separation, the residual polymer layer of the imprinted MR-I resist was removed using $O_2$ plasma reactive-ion etching. Metallization was accomplished using an electron beam evaporator by first depositing a 3 nm Ti adhesion layer followed by 50 nm of Au. Lift-off was performed by soaking the sample in acetone and using a low-power ultrasonic bath. After completion of lift-off, samples were rinsed with methanol and IPA and dried with $N_2$.

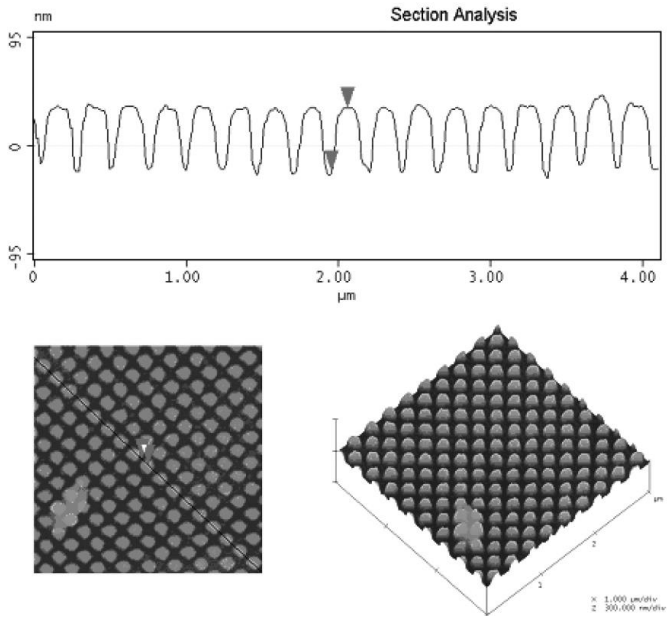


**Figure 4.1 AFM images and section of used Au NPAs.**

The AFM images and section of 120×130×50 nm Au nanorectangles with interparticle distance equal to 237 nm are depicted in Figure 4.1. It should be noted that AFM technique does not resolve the correct estimation of the distance between NPAs due to limitation related to the geometry of AFM tip.

**Methods**

All extinction measurements were taken using a Nikon TE300 Eclipse inverted microscope (20× objective with the numerical aperture 0.44) with transmitted light coupled into an Ocean Optics SD2000 fiber-coupled spectrometer using an achromatic lens (experimental setup is presented schematically in Figure 4.2).

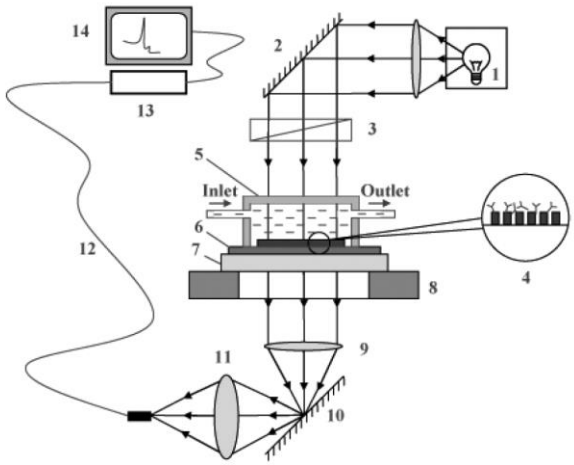


**Figure 4.2 Schematic presentation of the experimental set-up for extinction spectroscopy measurements. *1* – 100 W halogen source; *2*, *10* – mirrors; *3* – polarizer; *4* – surface nanostructures with a biomolecular layer: rectangular array with adsorbed IgG molecules; *5* – flow cell; *6* – glass-ceramic substrate; *7* – glass substrate; *8* – sample holder; *9*, *11* – lenses; *12* – fiber-optic cable; *13* – spectrometer; *14* – computer.**

All measurements were taken using normally incident light and referenced to unpatterned glass. A refractive index change was introduced by embedding the NPA in a DI:$H_2O$ water. Experiments were performed using the original LSPR sensor chip, wherein pyrex glass substrate (size about of 2×2 mm) modified with layer of NPAs was fixed on the surface of microscopic glass substrate (size 25×76 mm) and covered by a transparent 20 µl flow cell. For the real-time measurements of biomolecular interactions the peristaltic pump (Multiflex, USA, flowrate 10 µL/min) was used. The glycerol,

phosphate buffer saline (PBS) solution (pH = 7.4), bovine serum albumin (BSA), anti-BSA immunoglobulin (IgG) were purchased from Sigma-Aldrich.

**Results**

The nanoscale biosensors based on LSPR spectroscopy operate in the same manner as their SPR counterparts by transducing small changes in refractive index near the noble metal surface into LSPR response (a measurable wavelength shift response). The biosensors are liquid sensors that work in the real-time mode; therefore, first we tested NPA structures for their sensitivity to changes of the liquid environment refractive index. The glycerol-water solutions with various refractive indices were used for this aim. The refractive indices of these solutions were determined using the standard Abbe refractometer.

Measurements for the detection of refractive index changes were carried out in a flowing regime, with real-time monitoring of the wavelength (initial = 650 nm) shift. The results obtained for calibrated glycerol solutions clearly show that the optical extinction of the NPA structures is sensitive to the refractive index of the surrounding liquid medium. The results of the experiment are depicted in Figure 4.3. Close to linear dependence of the extinction shift on the refractive index was observed (see inset for Figure 4.3).

The measurements were performed for the right side of the extinction peak ($\lambda$ = 660 nm). It should be noted that we found a correlation between the chosen wavelength on our peak and the resulting response; however, during experiments there were some peculiarities related to the difference in a rate and direction of the wavelength shift for different points in the extinction peak branches. From our observations, it is most

preferable to use wavelengths found on the right side of the peak, however, this point requires additional study. The issue of the sensitivity of LSPR biosensors is rather complicated due to a confluence of many factors which include the electrodynamic interaction between nanostructures that decreases with an increase of interparticle distance and influences the shape as well as spectral position of the LSPR peak [26].

The nanorectangle NPA used in this study is characterized by in-plane lateral dimensions of 120 nm and 130 nm, uniformly oriented on a square lattice with a period of 237 nm. Even with such a minuscule anisotropy in these near-unity aspect ratio NPA constituents, the dichroism is readily observed (Figure 4.4) and the polarization dependent sensitivity was followed. This can imply a significant difference in the character of the electric field in the vicinity of the nanoparticles for different polarizations of the light source. This variation in LSPR response demonstrates that polarized light can be used for the optimization of the parameters of LSPR sensors produced by NIL.

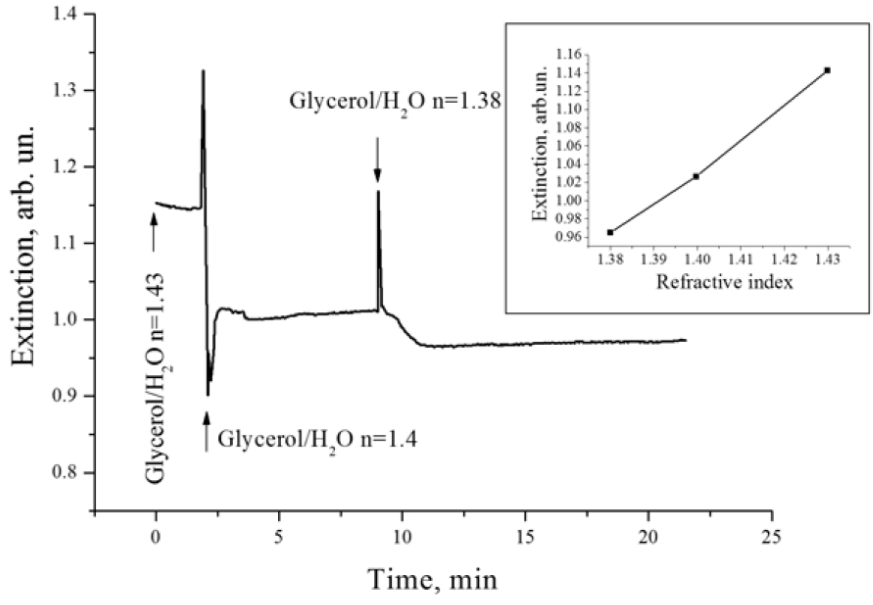


**Figure 4.3 The real-time kinetic dependence of extinction on bulk refractive index.**

Similar to conventional SPR, the wavelength position and shape of LSPR extinction peak influence the sensitivity of biosensor utilizing the plasmon resonance phenomenon. It is known that a more narrow peak, positioned at shorter wavelength, exhibits the lower sensitivity $S = \Delta\lambda/\Delta n$, where $\lambda$ is the peak center wavelength and n is the refractive index of the environment. However, due to necessity of computer treatments of extreme region in extinction spectra to define the exact wavelength peak position, a narrow peak appears as more suitable to obtain the lower "noise" of kinetic curve. Oppositely, the wide wavelength peak exhibits higher sensitivity, but, at the same time, a higher noise level. From this point of view, 3D-geometry and density of NPA on the surface of substrate should be optimized. The factor of polarization for NPAs is also important due to easy possibility to produce the asymmetric structures with high dichroism degree.

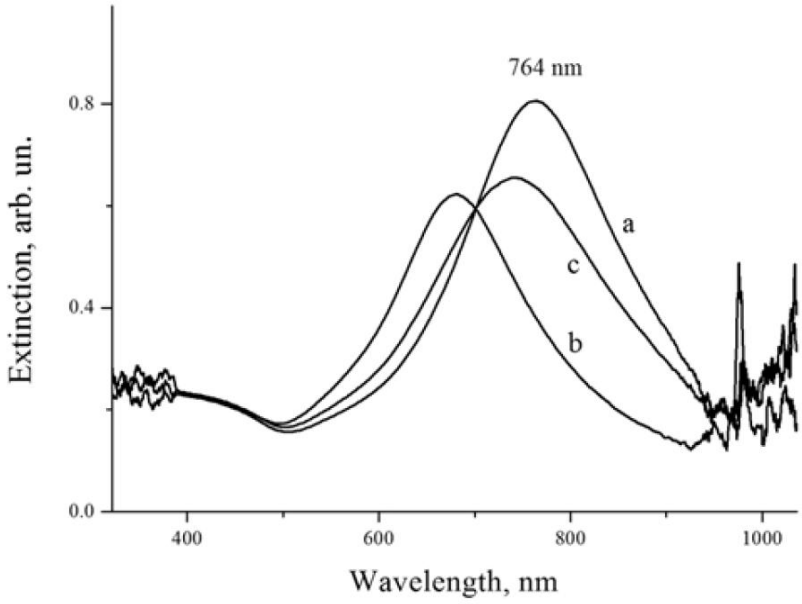


**Figure 4.4 Polarization extinction spectra for the nanoblock NPA with linear polarization of the incident light oriented along (a) the long axis (0°, longitudinal mode) and (b) short axis of the nanoblocks (90°, transverse mode). (c) The extinction spectrum for the case of 45° polarization.**

To estimate the kinetic response of LSPR biosensor on adsorption of real biological materials, we utilized the produced NPAs to detect the biospecific reaction between bovine serum albumin (BSA, $M_W \approx 60$ kDa) and anti-BSA immunoglobulin (IgG, $M_W \approx 150$ kDa). The results of experiment are depicted in Figure 4.5, where the real-time kinetic dependence of extinction for the specific reaction between BSA and immunoglobulin dissolved in PBS buffer solution with different concentrations of the PBS/anti-BSA solution is shown.

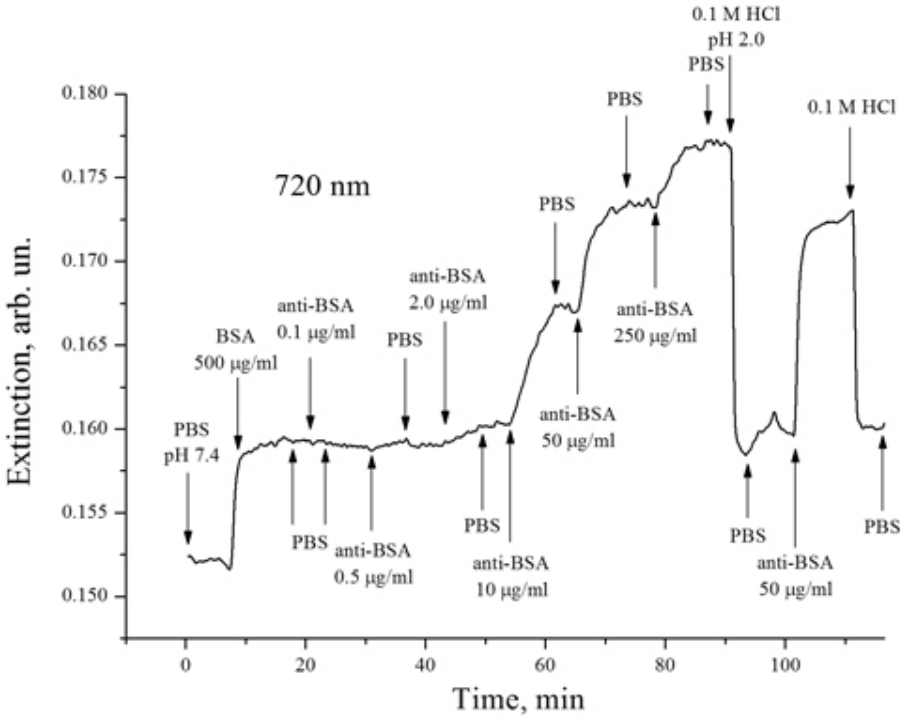


**Figure 4.5 The real-time kinetic dependence of extinction for the specific reaction BSA-anti-BSA with different concentrations of the PBS/anti-BSA immunoglobulin solution.**

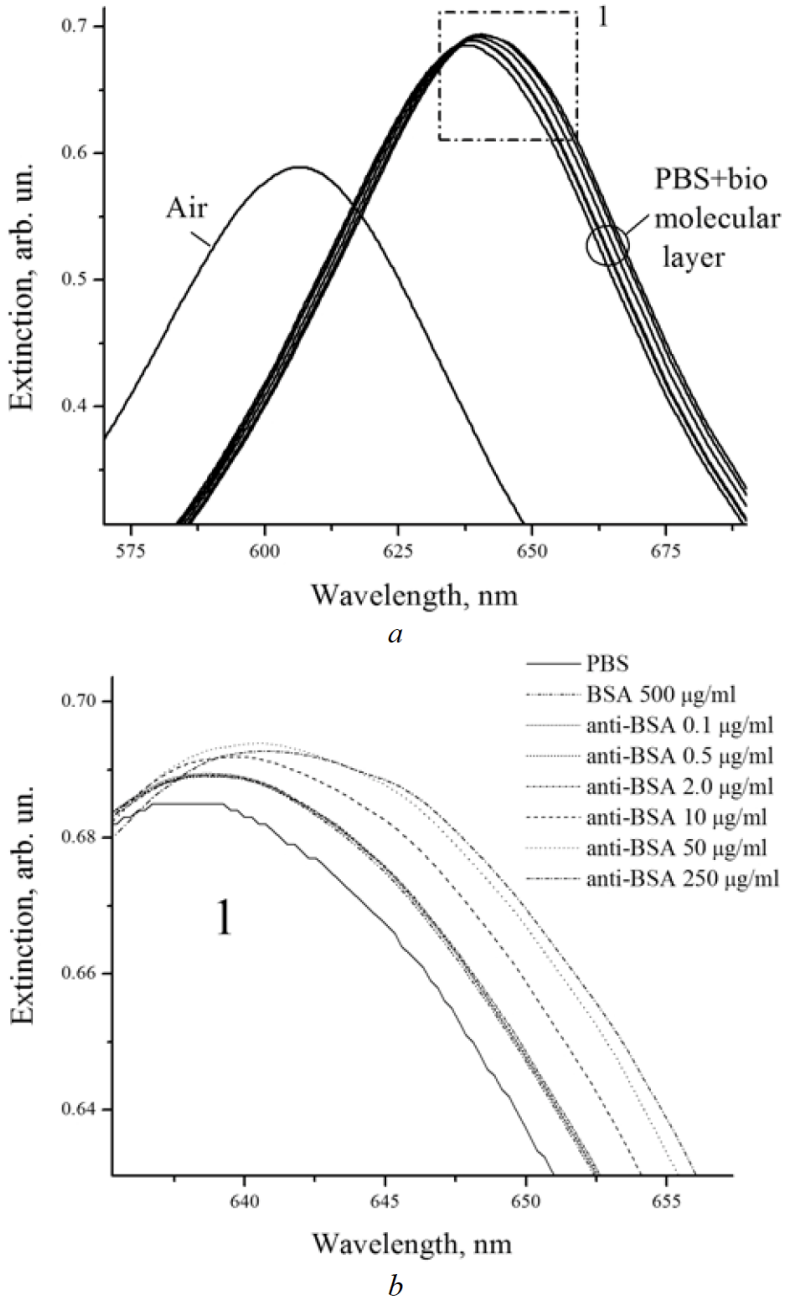


**Figure 4.6 (a) Extinction spectra for NPAs in air, in buffer solution and for various concentrations of PBS/anti-BSA immunoglobulin solution. (b) Magnified part of the spectral range 1.**

As one can see from Figures 4.5 and 4.6, at the beginning of the experiment the comparatively strong extinction shift was obtained for the PBS/BSA solution of 500

μg/ml concentration and, further, concentration dependent wavelength shift for IgG solutions beginning from 0.1 μg/ml. It is evident that a distinct response due to BSA-anti-BSA specific reaction arises at the injection of anti-BSA solution with concentration of 0.5 μg/ml. It should be noted that the smallest (0.1 μg/ml) concentration was not detected; this proves our assumption that the LSPR biosensor can be more suitable for registration of biomolecules with small molecular mass due to more developed Au surface comparatively with that in conventional SPR sensors and, respectively, due to possibility for small biomolecules, which easily penetrate and are adsorbed onto lateral faces, to fill the volume between nanostructures.

In addition, a high degree of specificity of the reaction was observed during the experiment after washing the IgG layer with 0.1 M HCl solution, when close to 100 % of antibody was removed, whereas BSA layer remained completely at the sensor surface. As evident from the abovementioned sensogram, the developed LSPR biosensor is completely able for regeneration and repeating the specific reaction.

**Conclusion**

A novel developed LSPR biosensor based on approach to fabricate large-area, uniformly-oriented noble metal NPAs using nanoimprint lithography was presented. With the increasing number of applications based on the field enhancements provided by metal NPs, we believe this method can be practically important for the serial production of homogenous nanostructure populations and biosensors based on them. The experimental and theoretical studies of NIL-produced noble metal NPAs possessing a variety of unique dimensional characteristics and related LSPR attributes are ongoing.

Au nanostructure NPA capability for detection of adsorption of biomolecules with different molecular weight in a real-time mode has been demonstrated in this work. The performed experiments show promising perspectives of the LSPR method for exploitation of NPA-structures as the basis for biomolecular detection and monitoring of specific biomolecular interactions.

## References


[1] U. Kreibig and M. Vollmer, *Optical properties of metal clusters*: Springer, 1995.

[2] J. F. Venger, A. V. Hončarenko, and M. L. Dmitruk, *Optics of small particles and disperse media*: Naukova Dumka, 1999.

[3] H. A. Atwater, S. Maier, A. Polman, J. A. Dionne, and L. Sweatlock, "The New "p–n Junction": Plasmonics Enables Photonic Access to the Nanoworld," *MRS Bulletin,* vol. 30, pp. 385-389, 2005/005/001 2005.

[4] A. M. Stefan, "Plasmonics - Towards Subwavelength Optical Devices," *Current Nanoscience,* vol. 1, pp. 17-22, 2005.

[5] B. K. Canfield, S. Kujala, M. Kauranen, K. Jefimovs, T. Vallius, and J. Turunen, "Remarkable polarization sensitivity of gold nanoparticle arrays," *Applied Physics Letters,* vol. 86, pp. -, MAY 2 2005.

[6] Y. Dirix, C. Bastiaansen, W. Caseri, and P. Smith, "Oriented pearl-necklace arrays of metallic nanoparticles in polymers: A new route toward polarization-dependent color filters," *Advanced Materials,* vol. 11, pp. 223-+, Feb 11 1999.

[7] C. L. Haynes and R. P. Van Duyne, "Dichroic optical properties of extended nanostructures fabricated using angle-resolved nanosphere lithography," *Nano Letters,* vol. 3, pp. 939-943, Jul 2003.

[8] M. D. Malinsky, K. L. Kelly, G. C. Schatz, and R. P. Van Duyne, "Nanosphere lithography: Effect of substrate on the localized surface plasmon resonance spectrum of silver nanoparticles," *Journal of Physical Chemistry B,* vol. 105, pp. 2343-2350, Mar 29 2001.

[9] J. J. Mock, M. Barbic, D. R. Smith, D. A. Schultz, and S. Schultz, "Shape effects in plasmon resonance of individual colloidal silver nanoparticles," *Journal of Chemical Physics,* vol. 116, pp. 6755-6759, APR 15 2002.

[10] J. J. Mock, D. R. Smith, and S. Schultz, "Local refractive index dependence of plasmon resonance spectra from individual nanoparticles," *Nano Letters,* vol. 3, pp. 485-491, APR 2003.

[11] K. H. Su, Q. H. Wei, X. Zhang, J. J. Mock, D. R. Smith, and S. Schultz, "Interparticle Coupling Effects on Plasmon Resonances of Nanogold Particles," *Nano Letters,* vol. 3, pp. 1087-1090, 2003/08/01 2003.

[12] A. Bouhelier, R. Bachelot, J. S. Im, G. P. Wiederrecht, G. Lerondel, S. Kostcheev, *et al.*, "Electromagnetic interactions in plasmonic nanoparticle arrays," *Journal of Physical Chemistry B,* vol. 109, pp. 3195-3198, Mar 3 2005.

[13] S. J. Oldenburg, G. D. Hale, J. B. Jackson, and N. J. Halas, "Light scattering from dipole and quadrupole nanoshell antennas," *Applied Physics Letters,* vol. 75, pp. 1063-1065, Aug 23 1999.

[14] L. J. Sherry, S. H. Chang, G. C. Schatz, R. P. Van Duyne, B. J. Wiley, and Y. N. Xia, "Localized surface plasmon resonance spectroscopy of single silver nanocubes," *Nano Letters,* vol. 5, pp. 2034-2038, Oct 2005.

[15] J. C. Riboh, A. J. Haes, A. D. McFarland, C. Ranjit Yonzon, and R. P. Van Duyne, "A Nanoscale Optical Biosensor: Real-Time Immunoassay in Physiological Buffer Enabled by Improved Nanoparticle Adhesion," *The Journal of Physical Chemistry B,* vol. 107, pp. 1772-1780, 2003/02/01 2003.

[16] R. G. Freeman, K. C. Grabar, K. J. Allison, R. M. Bright, J. A. Davis, A. P. Guthrie, *et al.*, "Self-Assembled Metal Colloid Monolayers: An Approach to SERS Substrates," *Science,* vol. 267, pp. 1629-1632, 1995.

[17] K. C. Grabar, R. G. Freeman, M. B. Hommer, and M. J. Natan, "Preparation and Characterization of Au Colloid Monolayers," *Analytical Chemistry,* vol. 67, pp. 735-743, 1995/02/01 1995.

[18] M. Serhiy and C. George, "Coupled planar silver nanoparticle arrays as refractive index sensors," *Journal of Optics A: Pure and Applied Optics,* vol. 8, p. S144, 2006.

[19] S. Y. Chou and P. R. Krauss, "Imprint lithography with sub-10 nm feature size and high throughput," *Microelectronic Engineering,* vol. 35, pp. 237-240, FEB 1997.

[20] M. T. Li, L. Chen, W. Zhang, and S. Y. Chou, "Pattern transfer fidelity of nanoimprint lithography on six-inch wafers," *Nanotechnology,* vol. 14, pp. 33-36, JAN 2003.

[21] A. D. McFarland and R. P. Van Duyne, "Single silver nanoparticles as real-time optical sensors with zeptomole sensitivity," *Nano Letters,* vol. 3, pp. 1057-1062, Aug 2003.

[22] N. Nath and A. Chilkoti, "A colorimetric gold nanoparticle sensor to interrogate biomolecular interactions in real time on a surface," *Analytical Chemistry,* vol. 74, pp. 504-509, Feb 1 2002.

[23] W. Knoll, "INTERFACES AND THIN FILMS AS SEEN BY BOUND ELECTROMAGNETIC WAVES," *Annual Review of Physical Chemistry,* vol. 49, pp. 569-638, 1998.

[24] P. Schuck, "USE OF SURFACE PLASMON RESONANCE TO PROBE THE EQUILIBRIUM AND DYNAMIC ASPECTS OF INTERACTIONS BETWEEN

BIOLOGICAL MACROMOLECULES," *Annual Review of Biophysics and Biomolecular Structure,* vol. 26, pp. 541-566, 1997/06/01 1997.

[25] V. Lozovski, "Electrodynamical interactions inside a system of nano-particles," *Physica E: Low-dimensional Systems and Nanostructures,* vol. 19, pp. 263-277, 8// 2003.

[26] S. M. Kachan and A. N. Ponyavina, "Spectral properties of close-packed monolayers consisting of metal nanospheres," *Journal of Physics: Condensed Matter,* vol. 14, p. 103, 2002.

[27] W. H. Yang, G. C. Schatz, and R. P. V. Duyne, "Discrete dipole approximation for calculating extinction and Raman intensities for small particles with arbitrary shapes," *The Journal of Chemical Physics,* vol. 103, pp. 869-875, 1995.

# Chapter 5

## Nanoimprinted Electrodes for Micro-fuel Cell Applications

### Introduction

Fuel cells are an attractive alternative to batteries for portable electronic devices. Micromachining methods hold promise for producing fuel cell structures with high degrees of materials utilization and low costs. Several approaches have been reported for the production of micro-fuel cells using micromachining techniques[1-3]. Most of these devices include micromachined fuel cell components combined with conventional macro-MEAs (membrane electrode assemblies). Morse et al. [4] and Taylor and Thompson [5] demonstrated micro-fuel cells with most of the components produced using micromachining methods. Catalyst structures produced via electrodeposition of Pt and Pd have also been demonstrated in a micro-fuel cell [6].

Towards improving the performance and lowering the cost of the electrodes, we report the use of nanoimprint lithography (NIL) to fabricate electrodes with high specific Pt surface areas. Nanoimprint lithography is an emerging lithographic technology that has applications for high-throughput patterning of nanostructures [7]. Based on the mechanical embossing principle, nanoimprint techniques can achieve pattern resolutions beyond the limitations set by light diffraction or beam scattering in other conventional techniques [7, 8]. In addition, NIL can be used to pattern nonflat surfaces without the need for planarization [9] . In this article, we report methods for using NIL to create fuel

cell electrodes. We will also demonstrate methods to use NIL to emboss nanostructures onto spin casted Nafion films as well as bulk Nafion 117. For the Nafion 117, a shadow mask was used and a thin film of Pt catalyst was deposited on top of the nanostructures at a wide angle which prevented the formation of a continuous film. This Nafion film was then incorporated into an MEA and evaluated in a fuel cell. To our knowledge, this is the first time this technique has been demonstrated for fuel cell applications.

**Methods**

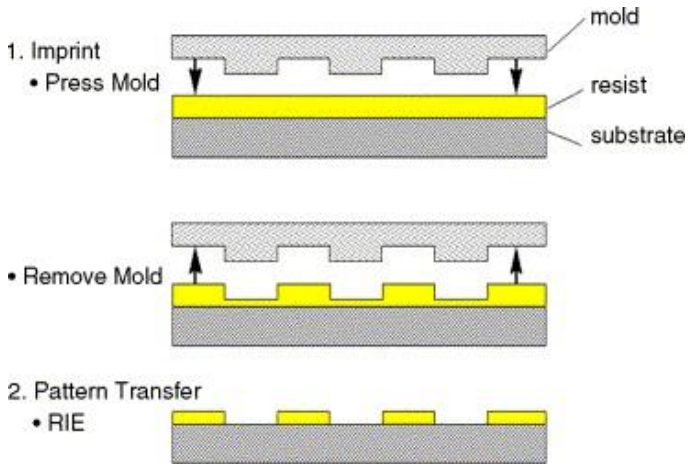


**Figure 5.1 Nanoimprint lithography process [40].**

## NIL Mold Fabrication

Fabrication of the electrodes and all of the nanoimprinting processes were conducted in the Lurie Nanofabrication Facility. Figure 5.1 illustrates the standard NIL process [8]. The one-dimensional $SiO_2$ grating mold used for electrode fabrication and Nafion embossing is characterized by a 1:1 duty cycle and 700 nm pitch. The flexibility of the NIL technique permits the simultaneous transfer of nanoscale features to a variety

of different substrates. Figure 5.2 illustrates $SiO_2$ molds that we have used for nanoimprinting. Results reported in this paper used the mold illustrated in Figure 5.2A.

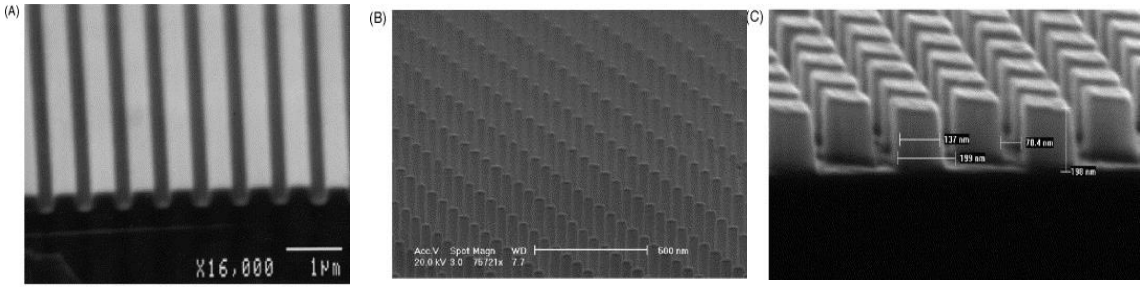


**Figure 5.2(A) SEM image of grating mold structure (1:1 duty cycle 700 nm period); (B) rod mold structure; (C) cube mold structure.**

## Nanoimprinted Electrodes

The nanoimprinted electrodes were fabricated on a single side polished P type 4 in. 〈1 0 0〉 silicon wafer. Following a standard pre-furnace clean, a 200 nm low pressure chemical vapor deposition (LPCVD) oxide was grown on the wafer to isolate the electrodes from the substrate. A 200 nm planar Au film was deposited using an electron beam (e-beam) evaporator (Enerjet Evaporator, pressure < $10^{-6}$ Torr) with a 3 nm Ti underlayer serving as an adhesion promoter. The wafers were then cleaved to appropriate sizes for the nanoimprint lithography step.

## Nanoimprint Lithography

The nanoimprint resist (Micro Resist Technology mr-I 8030; $T_g$ = 115 °C) was spin cast (250 nm) onto the freshly prepared substrate and baked using a hotplate (140 °C; 5 min) to remove residual solvent. The sample was then imprinted using a custom-built nanoimprinter (700 psi, 180 °C, 5 min), cooled to 55 °C and released from the mold. An electron beam deposited Cr mask layer was applied to the protruding lines

of the surface relief pattern using shadow evaporation at approximately 60° off normal. This step was included to help increase the fidelity of pattern transfer during residual polymer removal independent of the etch anisotropy and to create preferred undercut for liftoff processing. The residual polymer layer was removed using (RIE) reactive-ion etching (20 sccm $O_2$, 50 W, 20 mT).

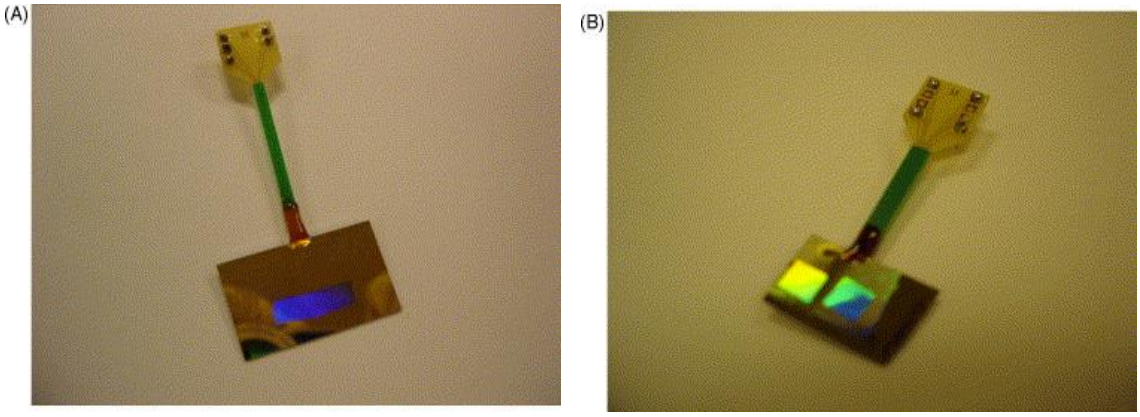


**Figure 5.3 (A) Pt nanostructured electrode 13 mm × 4 mm; (B) 2 Pt nanostructured electrodes 4.5 mm × 4.5 mm**

The Pt catalyst lines (5‑200 nm) were subsequently deposited using e-beam evaporation onto a 3 nm Ti adhesion layer through a shadow mask to produce a well-defined rectangular nanostructured surface. Metal and resist liftoff were accomplished using an acetone soak and gentle mechanical cleaning with a swab was used to remove any residual insoluble complex from the Pt and Au surfaces. Figure 5.3A illustrates an electrode with Pt nanobars (thickness: 50 nm) shown in the blue region which covered an active area of 13 mm × 4 mm. Figure 5.3B illustrates two electrodes fabricated on the same substrate. Both electrodes were electrically isolated and were used to verify the reproducibility of the shadow masks. The area of the shadow masks for these electrodes corresponds to a Pt area of 4.5 mm × 4.5 mm and thickness of 5 nm. The contrast in color for the electrodes corresponds to light diffracted at different angles due to the

grating pattern of the imprinted regions. Figure 5.4 is a scanning electron micrograph (SEM) of the Pt nanoimprinted electrodes. The width and pitch of the bars were determined to be 350 nm which corresponds to the 700 nm period grating mold (Figure 5.2A). The full dimensions of a single Pt bar in Figure 5.3A and B are 13 mm × 350 nm × 50 nm, and 4.5 mm × 350 nm × 5 nm, respectively.

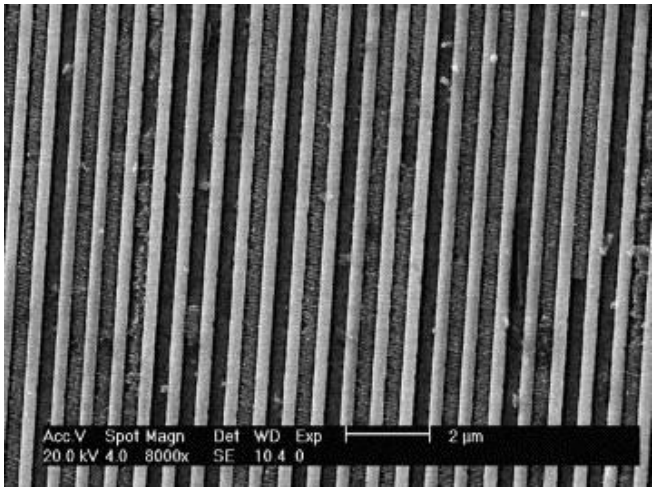


**Figure 5.4 SEM image of the Pt nanoimprinted electrodes.**

## Spin Cast Nafion Embossing

Nafion solutions (5% Aldrich) were spin cast onto pieces of oxide covered silicon. The thickness of the film was 500 nm and was calibrated at a spin speed of 500 rpm. The molds were pressed into the substrates at 900 psi and 135 °C for 5 min. These conditions yielded the best transfer of mold features to the thin films. Figure 5.5 illustrates results from embossing a Nafion thin film. The colored region identifies the imprinted sample area which is held at different angles to demonstrate light diffraction. The pattern

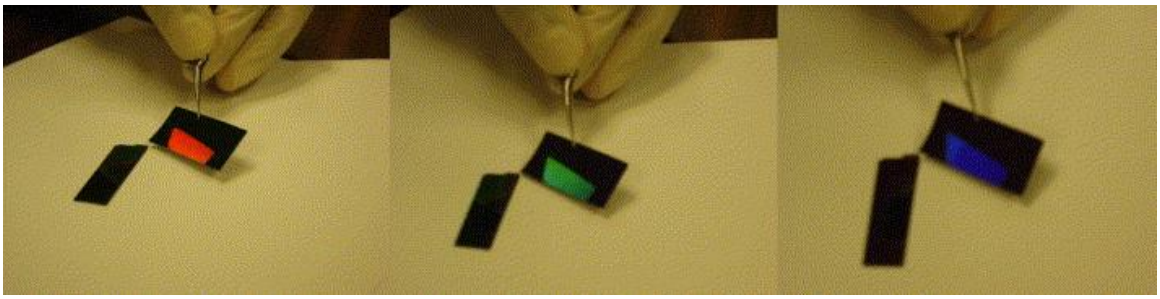

Figure 5.5 Nanostructured Nafion thin film.

transferred to these features was very uniform. Figure 5.6 shows an SEM cross-section of the imprinted Nafion film.

## Nafion 117 Embossing

The Nafion 117 films were cleaned using procedures that we have successfully used in the past. To remove organic impurities and to obtain the H+ form for use in the PEM fuel cell, the membranes were pretreated by boiling the pieces in 50 vol.% $HNO_3$ and deionized water for 1 h. The films were then rinsed in boiling deionized (DI) water for 30 min, boiled in a 0.5 M $H_2SO_4$ solution for 30 min, and boiled twice in DI water for 30 min. The membranes were subsequently stored in DI water until ready for use.

A hydrated Nafion 117 membrane was placed onto a clean Si substrate and dried using a stream of $N_2$ to remove any visually observable water droplets from the surface. The mold was then placed directly onto the membrane and inserted into the nanoimprinter chamber. A pressure of 900 psi was immediately applied to the sample to minimize membrane buckling due to loss of moisture as the chamber temperature was increased to 150 °C. The film was held at 150 °C for 5 min then cooled to 55 °C. The mold was separated from the membrane and a thin film of Pt (7.5 nm) was deposited onto the protruding lines of the embossed pattern. A shadow mask was used to ensure that the Pt was deposited only on the embossed region, and the film was oriented at an angle from

the Pt target to maximize Pt coverage on the peaks and valleys of the embossed (nanostructured) region.

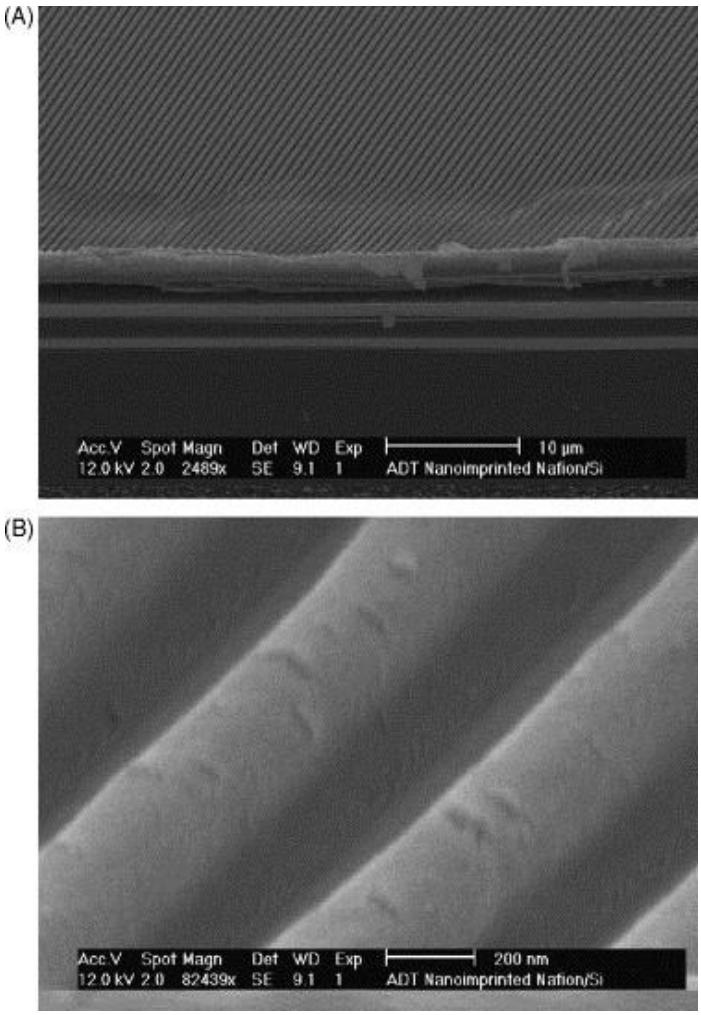


**Figure 5.6 (A) SEM cross-section of Nafion® nanostructured thin film; (B) enlarged SEM cross-section of Nafion® nanostructured thin film**

## Electrode Characterization

The catalyst structures (fabricated on gold covered $SiO_2$ on silicon; Figure 5.3 and Figure 5.4) were characterized electrochemically using cyclic voltammetry in a half-cell three electrode system containing 0.5 M $H_2SO_4$electrolyte versus a Ag/AgCl reference electrode (Bio Analytic Systems). The electrolyte solutions were prepared from Milli-Q® water and sulfuric acid (Fischer CMOS grade). Prior to carrying out an

experiment the electrolyte in the three-electrode chemical cell was purged with Argon for 30 min.

The electrode potential was controlled by a PAR (Prince Applied Research) Model 273 potentiostat which was controlled using CorrWare Electrochemical Experiment Software developed by Scribner Associates, Inc. The counter electrode was a Pt wire attached to a Pt mesh. Potentials are quoted versus the Ag/AgCl reference electrode. Before each experiment the counter and working electrodes were thoroughly rinsed in Milli-Q® water.

**Fuel Cell Tests**

Membrane electrode assemblies incorporating the standard electrode and the embossed Nafion 117 anode side with a Pt thin film were fabricated using E-tek (ELAT V3.1 double side automated) gas diffusion layers (GDLs). The catalyst ink solutions were prepared using a Johnson Matthey Pt/C catalyst (20 wt.% Pt loading). The cathode catalyst layers with Pt loadings of 0.5 mg $cm^{-2}$ were prepared using an ink solution consisting of 68% Pt/C, 20% Nafion, and 12% PTFE by weight.

The standard MEA anode consisted of 75% Pt/C and 25% Nafion with a Pt loading of 0.5 mg $cm^{-2}$. The nanoimprinted MEA had a Pt anode loading of 8.0 $\mu$ g $cm^{-2}$ and a standard cathode. The MEAs were fabricated by hot pressing the electrolyte membrane between two GDLs at 135 °C for 5 min at a pressure of 10 MPa. The MEAs were tested in a single fuel cell housing. The MEAs were conditioned overnight until a steady state current was achieved at a potential of 0.6 V. The temperature of the fuel cell was 80 °C and the anode and cathode saturators were set at 90 °C which yield reactant

gases with 100% relative humidity. The flow rates of the humidified hydrogen and oxygen were held constant at 100 sccm using mass flow controllers.

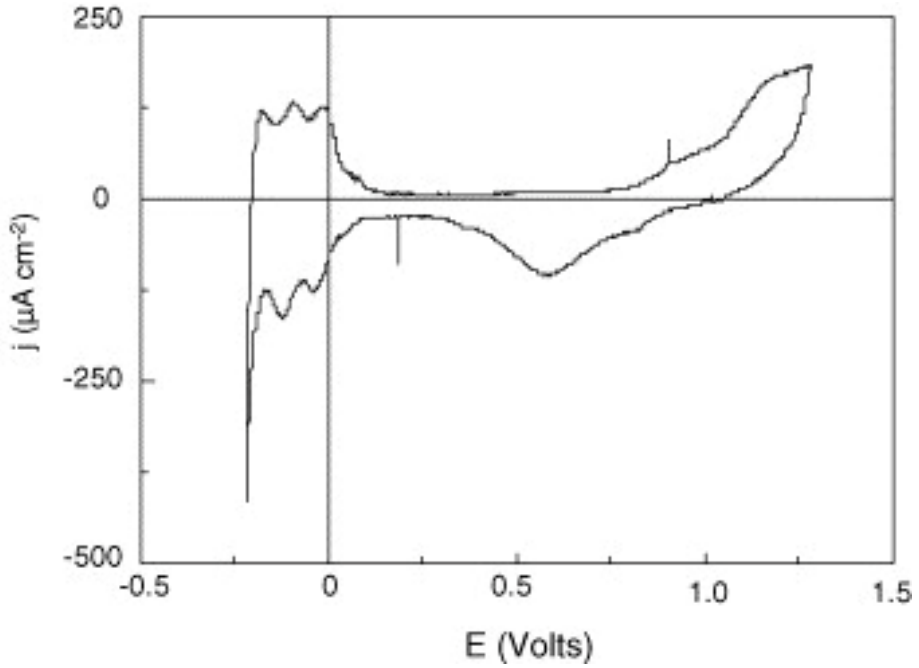


**Figure 5.7 Cyclic voltammogram of Pt nanostructured electrode.**

A characteristic voltammogram for the nanoimprinted electrode on $SiO_2$ (on silicon) is presented in Figure 5.7. The features are typical of polycrystalline Pt. The thickness of the Pt layer was 50 nm based on on-line monitoring using a frequency-shift measurement from a resonating crystal. The hydrogen desorption region was integrated to determine the coulombic charge (corrected for the double-layer capacitance of the Pt and Au/Ti support) for each electrode and yielded a maximum electrochemical active surface (EAS) area of 1.5 $m^2$ $g^{-1}$ Pt. These EAS values are higher than those for micro-fuel cell electrodes we previously reported [5].Our previous electrodes were prepared using standard micromachining methods and typically had EAS areas of ~0.3 $m^2$ $g^{-1}$ Pt. These EAS areas are lower than those for typical fuel cell catalysts which range from 65 to

100 $m^2$ $g^{-1}$ for lower-loaded catalysts (e.g. 20 wt.% Pt/Vulcan XC72) [10]. The EAS areas for electrodes produced using the NIL method will be improved with further development.

Figures 5.5 and 5.6 demonstrate the results of imprinting nanostructures directly onto Nafion thin films. The features possess a distinct 700 nm period. The surface edges of the embossed film appeared to be rounded which suggests that the films relaxed (and/or expanded) after the compression step. This may be due to the fact that the films were embossed immediately after casting without curing. The consistent color diffraction in the imprinted region suggests that the rest of the film was not compromised from this process. The embossing of nanostructures onto Nafion thin films holds promise for a variety of new micro-fuel cell designs. In addition, micro-fluidic devices that exploit the proton selectivity of Nafion for reactions and/or separations could be possible. We are presently investigating the viability of these options.

The embossing of Nafion 117 is a fairly simple process. Our earlier attempts focused on casting a uniform layer of nanoimprint resist on the surface of the membranes. This proved to be difficult due to buckling of the membrane as it was either dried or absorbed solvent from the resist layer. The direct embossing of Nafion has the advantage of controlled surface modification without chemical contamination. Previously we observed that chemicals used in modern micromachining processes (e.g. photoresist, photoresist developer, solvent, etc.) can negatively impact the performance of an MEA. Since lift-off and post-chemical treatment was not required for this process, a shadow mask was created to selectively deposit Pt over the embossed nanostructured features. For comparison, O'Hayre et al. reported a peak in performance for Pt sputtered thin films

(5-10 nm) on top of a smooth Nafion 117 surface [11]. The maximum power was several orders of magnitude higher than thinner or thicker films. Figure 5.8 illustrates a

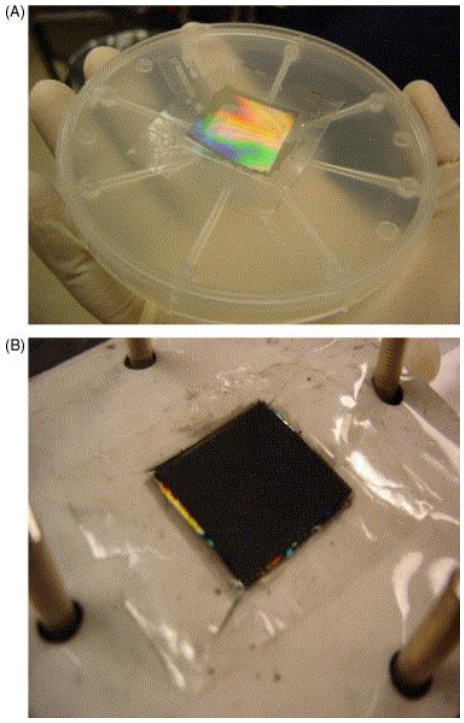


**Figure 5.8 (A) Illustration of Pt on embossed Nafion 117 film; (B) embossed Nafion 117.**

MEA 7.5 nm Pt film deposited on top of an embossed (nanostructured) Nafion 117 surface. The imprinted patterns were consistent with the Nafion thin films shown in Figure 5.6.

The membrane was fabricated into an MEA and the performance was compared to an MEA prepared using conventional materials. The polarization curves are illustrated in Figure 5.9. Although the peak power density of the nanoimprinted MEA was

123 mW $cm^{-2}$, which was lower than that for the conventionally prepared MEA (410 mW $cm^{-2}$), the Pt utilization for the former was 15,375 mW $mg^{-1}$ Pt compared to

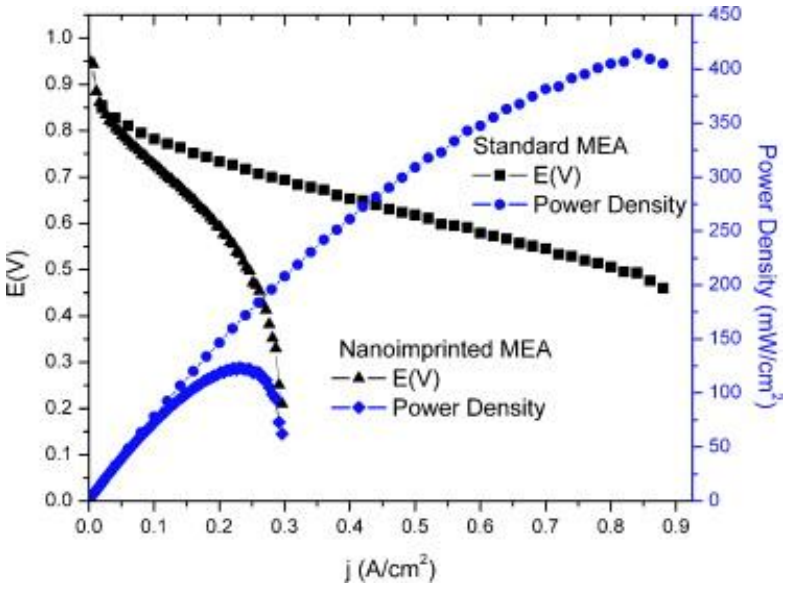


**Figure 5.9 Polarization curves of standard MEA and nanoimprinted MEA.**

820 mW $mg^{-1}$ Pt for the conventional electrode. These values were determined by dividing the peak power density by the Pt loadings for the anode (conventional MEA, 0.5 mg $cm^{-2}$; MEA with nanoimprinted electrode, 8 µg $cm^{-2}$).

Further characterization of the Pt on the nanoimprinted Nafion is underway and will be presented in a follow-up paper. The added areas from the Pt on the sidewalls of the nanostructures could contribute to increased performance over a planar surface. For instance for the structure used in this study (Figure 5.2A), the available added surface area is twice the amount of the planar surface. The improvement of a Pt film deposited onto Nafion achieved with this method is also consistent with improvements demonstrated by Cha et al. In this work, MEAs with sputtered films of Pt (deposited on top of the catalyst layer) showed an increase in performance compared to standard

MEAs [12]. The conclusion was that a higher concentration of Pt either near the GDL or Nafion layers increased performance of the catalyst layer.

**Discussion**

In order to improve the performance of micro-fuel cells, there will need to be an increase in the EAS area. This observed difference in EAS values (between standard Pt/C catalysts and Pt thin films) is directly related to overall fuel cell performance. In the micro-fuel cell research highlighted by Nguyen and Chen, it can be observed that the peak power densities of thin film electrode micro-fuel cells show lower (several orders of magnitude) performance compared to micro-fuel cells made with conventional catalysts [13].

Thin film electrodes that are CMOS compatible offer the possibility of fabricating the entire system using standard micromachining techniques. As a result, we believe that the same cost advantages realized in the integrated circuit industry could translate into reduced costs for fuel cells. The micro-fuel cells could also be fabricated with control circuitry and other electronic components which is not presently possible with lithium ion batteries.

Although circumventing the 2D characteristics of existing catalyst deposition techniques (i.e. sputtering, e-beam evaporation) would be attractive, a low cost method may exist where nanoimprinting could play an important role. For example, the control of catalyst particle size and orientation through the use of NIL could be a useful way to construct model catalysts. In addition, with the precise control of thin film thickness available using micromachining facilities coupled with smaller feature sizes available

from NIL, the exploitation of unique material properties available at the nanoscale could be further realized.

## Conclusion

In summary, we have fabricated electrodes with Pt nanostructures using the NIL method. The Pt nanostructures were active for hydrogen oxidation and the material was polycrystalline. We also demonstrated a simple method of embossing nanostructures directly onto Nafion thin films which could be used for the next generation MEMs (microelectromechanical systems) devices exploiting the material properties of an ionselective membrane. An embossed Nafion 117 film with Pt deposited on the nanostructures was fabricated into an MEA and demonstrated to be active. The catalyst layer on the embossed nanostructured Nafion had a significantly higher Pt utilization than a conventional catalyst layer.

## References


[1] S. C. Kelley, G. A. Deluga, and W. H. Smyrl, "Miniature fuel cells fabricated on silicon substrates," *AIChE Journal,* vol. 48, pp. 1071-1082, 2002.

[2] J. P. Meyers and H. L. Maynard, "Design considerations for miniaturized PEM fuel cells," *Journal of Power Sources,* vol. 109, pp. 76-88, 2002.

[3] R. O'Hayre, T. Fabian, S. J. Lee, and F. B. Prinz, "Lateral ionic conduction in planar array fuel cells," *Journal of the Electrochemical Society,* vol. 150, pp. A430-A438, 2003.

[4] J. D. Morse, A. F. Jankowski, R. T. Graff, and J. P. Hayes, "Novel proton exchange membrane thin-film fuel cell for microscale energy conversion," *Journal of Vacuum Science and Technology A: Vacuum, Surfaces and Films,* vol. 18, pp. 2003-2005, 2000.

[5] A. D. Taylor and L. T. Thompson, *IEEE Solid State Sensors and Actuators Workshop,* 2004.

[6] R. S. Jayashree, J. S. Spendelow, J. Yeom, C. Rastogi, M. A. Shannon, and P. J. A. Kenis, "Characterization and application of electrodeposited Pt, Pt/Pd, and Pd catalyst structures for direct formic acid micro fuel cells," *Electrochimica Acta,* vol. 50, pp. 4674-4682, 2005.

[7] L. J. Guo, "Recent progress in nanoimprint technology and its applications," *Journal of Physics D: Applied Physics,* vol. 37, pp. R123-R141, 2004.

[8] S. Y. Chou, P. R. Krauss, and L. Kong, "Nanolithographically defined magnetic structures and quantum magnetic disk (invited)," *Journal of Applied Physics,* vol. 79, pp. 6101-6106, 1996.

[9] L. R. Bao, X. Cheng, X. D. Huang, L. J. Guo, S. W. Pang, and A. F. Yee, "Nanoimprinting over topography and multilayer three-dimensional printing," *Journal of Vacuum Science and Technology B: Microelectronics and Nanometer Structures,* vol. 20, pp. 2881-2886, 2002.

[10] T. R. Ralph, G. A. Hards, J. E. Keating, S. A. Campbell, D. P. Wilkinson, M. Davis, *et al.,* "Low cost electrodes for proton exchange membrane fuel cells: Performance in single cells and Ballard stacks," *Journal of the Electrochemical Society,* vol. 144, pp. 3845-3857, 1997.

[11] R. O'Hayre, S. J. Lee, S. W. Cha, and F. B. Prinz, "A sharp peak in the performance of sputtered platinum fuel cells at ultra-low platinum loading," *Journal of Power Sources,* vol. 109, pp. 483-493, 2002.

[12] S. Y. Cha and W. M. Lee, "Performance of proton exchange membrane fuel cell electrodes prepared by direct deposition of ultrathin platinum on the membrane surface," *Journal of the Electrochemical Society*, vol. 146, pp. 4055-4060, 1999.

[13] N. T. Nguyen and S. H. Chan, "Micromachined polymer electrolyte membrane and direct methanol fuel cells - A review," *Journal of Micromechanics and Microengineering*, vol. 16, pp. R1-R12, 2006.

# Chapter 6

## Discussion and Future Works

The relevance of NIL to basic nanoscience research in a myriad of fields such as biotechnology, energy storage/conversion, photonics, and optoelectronics has been demonstrated over the last 20 years. The community of scientists and engineers working in the field of nanotechnology continue to devise new extensions of NIL that meet unique demands of particular applications. The ability to produce nanostructures in a large-area, high-throughput manner has allowed NIL to play a critical role in reducing the cost of working at the nanoscale and thereby affording contributions from a larger research community.

This thesis focuses on the role of NIL in the exciting fields of plasmonics, biotechnology and energy conversion. In chapter 2, we demonstrated NIL to be a viable method to produce arrays of plasmonic nanoparticles using one-dimensional grating molds in a double imprint approach. The resulting nanoblock molds possessed a variety of structural motifs based on the relative orientation of the two imprints. Among the properties studied, NPAs were characterized by their plasmon resonance wavelength, peak width, and optical dichroism. Tunability of the NPA plasmonic response for a specific material composition (e.g Au) was demonstrated by changing the nanoparticle height (i.e. thickness of evaporated metal film). It was found that increased particle height resulted in a more blue-shifted (i.e shorter wavelength) response. Work by Schatz

et. al. has demonstrated the role of electronic surface scattering when NP dimensions are on the order of the electron mean free path of the material [1]. Dampening of the response due to surface scattering effects were found to be negligible beyond 10 nm NPA heights.

Further flexibility in tuning the plasmonic wavelength was found by leveraging the thickness of the Ti adhesion promoter which was originally intended to allow more robust adhesion of the noble metal NPs to the glass substrates. The addition of only 1nm of Ti caused a significant shift for both Au and Ag NPs. Based on minimization of the FWHM for the plasmonic peak, it was found that 1 nm of Ti was the ideal adhesion layer thickness. While additional Ti allowed for further red-shifting of the plasmonic response, it also caused a significant dampening of the overall response. This can be attributed to the significant differences in the Fermi energy of the two metals that alter the overall free electron density of the composite NP.

Given the uniformity of the orientation of the constituent NPs with the array, the optical dichroic properties of the NPAs were assessed. The extent of the dichroism as determined by the wavelength difference between maximum and minimum plasmonic wavelengths was found to decrease with increased NP height. For example, 10nm Au NPs possessing an optical dichroism of 75 nm while 50 nm Au NPs only exhibited optical dichroism of 30 nm. This aspect of polarization sensitivity allows the overall NPA plasmonic response to be optimized to meet the needs of a specific application.

It should be noted that increasing the aspect ratio of the NPs will also enhance the optical dichroic properties of the NPA. However, it comes at the expense of accessing intermediary plasmonic states of the NPA. This is demonstrated by our nanorod

structures (~3:1 aspect ratio) where the variation of the incident linear polarization primarily causes the alternate excitation or suppression of longitudinal and transverse plasmonic modes. This causes a significant gap of accessible plasmonic wavelengths. Alternatively, our near-unity aspect ratio NPAs show the ability to access a continuum of plasmonic wavelengths by small angular changes in the incident linear polarization relative to the long and short axis of the NP. This tight control of the plasmonic wavelength through polarization affords greater tolerances in the various process steps (e.g. etching and metallization) by providing a means to compensate for unintended differences between the targeted and actual wavelengths with unpolarized light.

Additionally, the large-area NPA resulting from our fabrication approach allowed the interrogation of the plasmonic modes both in-plane and out-of-plane using obliquely incident polychromatic light. It was found that the plasmonic wavelength of the NPA could be blue-shifted when changing from normal incidence to oblique incidence. This effect is not only the result of the modification of the plasmonic response of each constituent NP but also influenced by changes in the coupling of the NPs. Previous work by Hicks demonstrated the role of radiative coupling, damping and retardation effects in EBL patterned NPAs through the calculation of a lattice sum which qualitatively captures the modification of the NPA plasmon resonance relative to the single particle response for changes in incident polarization vector and lattice spacing [2]. It was generally found that a decrease in lattice spacing caused a blueshift in the peak wavelength.

The ability of the NIL fabricated NPAs to detect refractive index changes was assessed by depositing a dielectric ($SiO_2$). Consistent with previously reported studies, our NPAs demonstrated a red shift in plasmonic peak wavelength with an increase of the

dielectric overlayer. This approach also showed a reduced sensitivity to dielectric changes further away from the particle surface which resulted in a saturation of NPA response for layers in excess of ~30 nm for both Au and Ag. This characteristic distant defines the effective sensing volume and thus also sets an upper limit on the ability of the NPA to detect larger biomolecular complexes that are unable to densely fill this volume.

It should be noted that this approach sets an upper limit on the detection sensitivity of NPA if utilized to transduce biomolecular interaction. This is due to the fact that surface coverage of biomolecules will never reach the complete coverage found using deposited adlayers of inorganic materials such as $SiO_2$. Additionally, the change of the refractive index is much larger due to the displacement of an air ambient (n=1) with the higher refractive $SiO_2$ ($n$ = 1.46) while a scheme to detect biomolecular interactions will require an initial aqueous ambient ($n$ = 1.33) that greatly reduces the index contrast resulting from the addition of biomolecules to the surface.

While we successfully demonstrated the ability to detect the real-time binding of a high-affinity antibody-antigen interaction aBSA:BSA, one ideal use of the NIL-produced plasmonic sensor is for point-of-care diagnostics. Recent work by Chen et.al. measuring cytockine concentrations using a microarray of NPs with integrated microfluidics further highlights the potential of NIL-produced NPAs. Through the use of dark-field microscopy, the rapid detection of was realized [3]. While the microarray spots were composed of diffuse nanorods, the ability to utilize homogeneous, uniformly-oriented NPAs should further improve the limit of detection (LOD) of the overall system.

The extension of NIL through its use of patterning functional polymer substrates was demonstrated in Chapter 5 with the nanopatterning of a proton exchange membrane

to enhance the performance of a microfuel cell. This approach highlights the endless opportunities for NIL play a role in patterning novel polymers for a variety of applications. Similar to the work to development of UV-sensitive resist systems that have afforded high-throughput, full-wafer imprints, many existing applications that benefit from NIL are positioned to be extended.

For example, one of the primary challenges to utilizing NIL-produced NPAs as transducers is the development of novel polymer chemistries to functionalize the constituent nanoparticles. Molecularly imprinted polymers (MIPs) has received considerable attention due to their ability to only allow targeted molecular constructs to integrate within the polymer matrix in a manner similar to a lock and key [4, 5]. Additionally, there have been various demonstrations of stimulus-responsive polymers. In response to environmental changes (e.g. pH), stimulus responsive polymers are able to swell or contract [6]. Identifying fabrication schemes that will allow these polymers to alter the distance between plasmonic NPs could offer a means to transduce these environmental changes.

Given the ubiquitous role that NIL continues to play in both basic science and translational research, it is clear that its utility will continue to grow. It is certainly well-positioned to continue to enhance existing applications and provide commercially-viable pathways for the creation of low-cost, high-throughput nanopatterned systems.

## References


[1] K. L. Kelly, E. Coronado, L. L. Zhao, and G. C. Schatz, "The Optical Properties of Metal Nanoparticles: The Influence of Size, Shape, and Dielectric Environment," *The Journal of Physical Chemistry B,* vol. 107, pp. 668-677, 2003/01/01 2003.

[2] E. M. Hicks, S. L. Zou, G. C. Schatz, K. G. Spears, R. P. Van Duyne, L. Gunnarsson, *et al.,* "Controlling plasmon line shapes through diffractive coupling in linear arrays of cylindrical nanoparticles fabricated by electron beam lithography," *Nano Letters,* vol. 5, pp. 1065-1070, Jun 2005.

[3] P. Chen, M. T. Chung, W. McHugh, R. Nidetz, Y. Li, J. Fu, *et al.,* "Multiplex Serum Cytokine Immunoassay Using Nanoplasmonic Biosensor Microarrays," *ACS Nano,* vol. 9, pp. 4173-4181, 2015/04/28 2015.

[4] J. O. Mahony, K. Nolan, M. R. Smyth, and B. Mizaikoff, "Molecularly imprinted polymers—potential and challenges in analytical chemistry," *Analytica Chimica Acta,* vol. 534, pp. 31-39, 4/4/ 2005.

[5] Z. Iskierko, P. S. Sharma, D. Prochowicz, K. Fronc, F. D'Souza, D. Toczydłowska, *et al.,* "Molecularly Imprinted Polymer (MIP) Film with Improved Surface Area Developed by Using Metal–Organic Framework (MOF) for Sensitive Lipocalin (NGAL) Determination," *ACS Applied Materials & Interfaces,* vol. 8, pp. 19860-19865, 2016/08/10 2016.

[6] C. de las Heras Alarcón, S. Pennadam, and C. Alexander, "Stimuli responsive polymers for biomedical applications," *Chemical Society Reviews,* vol. 34, pp. 276-285, 2005.